Politecnico di Torino



Master of Science in Georesources and Geoenergy Engineering

Numerical Modeling and Prediction of Wellbore Stability in Anisotropic Shale Formations

Supervisors:

Deangeli Chiara

Karimian Mobarakeh Monireh

Candidate:

Radja Karim

Ringraziamenti

All'interno di questa tesi, questo paragrafo sarà il solo a essere scritto in italiano.

Il primo ringraziamento va a Dio, per avermi dato la forza di affrontare questa sfida. Desidero poi ringraziare tutti i miei professori, e in particolare la Professoressa Chiara Deangeli, per avermi guidato e sostenuto con competenza e disponibilità durante la stesura di questo lavoro.

Un ultimo ringraziamento, il più sentito, va ai miei genitori, alla mia famiglia, alla mia fidanzata, agli amici, qui in Italia e in Algeria e a Khalil grazie per esserci sempre stati.

Abstract

Shales represent the most common sedimentary formations encountered during drilling operations, accounting for many wellbore instability issues. This difficulty comes from the anisotropic nature of shales, its layered fabric makes it stiffer and stronger along the bedding than across it, but many wellbore stabilities practice treats shale as an isotropic Mohr-Coulomb material. In This work, a numerical modelling was carried out to study the effect of anisotropy when treating wellbore stability problems, using the Cretaceous Qingshankou shale of the Songliao Basin as the case study. A wellbore was modelled in FLAC2D with five constitutive models of increasing complexity, from an isotropic linear elastic rock to a transversely isotropic elastic rock that can slip along its bedding. All five share the same grid, far-field stresses, pore pressure and mud pressure, so that any difference between these models comes from the material characteristics. The isotropic elastic model was first checked against the Kirsch solution for grid validation, and results were acceptable. The results of simulation pointed out three major points: first elastic anisotropy raises the hoop stress at the most loaded point on the wall enough to carry it from below the matrix strength to above it. Secondly, at the mud pressure that keeps the intact rock just at the edge of yielding, the bedding planes are already slipping over wide sectors of the wall, and a mud weight chosen only from the isotropic criterion would be unsafe. Finally, the excess pore pressure generated in the early hours after drilling forms a dipole around the hole that erodes the effective stress exactly where shear failure starts, but its magnitude ranks the models in the opposite order to their wall stress, so it cannot be read as a stability indicator alone. A comparison with Tournemire shale shows that the Songliao matrix is stronger than the Tournemire matrix, meanwhile the Songliao bedding is weaker relative to that matrix, relying only on matrix strength and ignoring the beddings can be misleading and can introduces significant errors into wellbore stability studies.

Keywords: wellbore stability, transversely isotropic shale, FLAC2D, weakness plane model, undrained pore pressure, Songliao Basin, mud weight window.

Table of Contents

1. Introduction **1**

1.1 The Evolving Global Energy Landscape 1

1.2 Shale as a Transversely Isotropic Rock 2

1.3 Scope and Structure 4

2. Wellbore Stability Fundamentals **6**

2.1 Stress Redistribution During Drilling 6

2.2 Effective Stress and Pore Pressure 7

2.2.1 Terzaghi's Principle 7

2.2.2 Drained and Undrained Conditions 7

2.3 In Situ Stresses and Pore Pressure 8

2.4 The Lamé Problem 9

2.5 The Kirsch Problem 10

2.6 Failure Criteria 12

2.6.1 Tensile Failure 12

2.6.2 Shear Failure 12

2.6.3 Mohr-Coulomb Criterion 12

2.6.4 Weakness Plane Model (WPM) 13

2.6.5 Modified Hoek-Brown Criterion 13

2.7 Mud Pressure and Mud Weight Window 14

3. Songliao shale: geological and geomechanical context **16**

3.1 Depositional settings: 16

3.2 Interpretation of laboratory tests: 17

4. Numerical Modeling with FLAC2D **20**

4.1 Introduction to FLAC2D 20

4.2 Model Setup: DONUT Grid and Boundary Conditions 20

4.3 Constitutive Models 23

4.3.1 ILE - Isotropic Linear Elastic 23

4.3.2 TIE - Transversely Isotropic Elastic 24

4.3.3 ILE-MC - Isotropic Mohr-Coulomb 25

4.3.4 UBI - Ubiquitous Joint 25

4.3.5 CANISO - Transversely Isotropic Elastic with Weak-Plane Slip 26
4.4 Simulation Plan 27
5. Results and Discussion **28**
5.1 Validation of the Numerical Model 28
5.1.1 Dry Protocol 29
5.1.2 Undrained Protocol 30
5.1.3 External Benchmark 32
5.2 Elastic Anisotropy: the TIE Model 33
5.3 Matrix Plasticity: the ILE - MC Model 36
5.4 Bedding Plane Slip: the UBI Model 39
5.5 Anisotropic Elasticity with Weak-Plane Slip: the CANISO Model 42
5.6 Comparison of the UBI and CANISO models 45
5.7 Mud Weight Window and Drilling Implications 47
5.7.1 Sensitivity to Mud Pressure 48
5.7.2 Practical Implications 49
5.8 Cross Model Synthesis 50
5.9 Comparison with Other Shales 51
5.10 Contribution and Limitations 53
6. Conclusions **56**
References **58**

List of Tables

Table 3.1 Average whole-rock mineralogy of the Qingshankou (K2qn1) oil shale and mudstone, southern Songliao Basin 15
Table 4.1 Common parameters of the numerical model setup 21
Table 4.2 Hydraulic protocol and grid configuration 22
Table 4.3 ILE material parameters 23
Table 4.4 TIE elastic parameters 23
Table 4.5 ILE-MC material parameters 24
Table 4.6 UBI/CANISO joint (weak plane) parameters 25
Table 4.7 Summary of the five constitutive models used in this thesis ... 25
Table 5.1 ILE, dry protocol: FLAC2D results at the borehole wall against the Kirsch solution 28
Table 5.2 ILE, undrained protocol (pf = 11 MPa, pw = 12 MPa): FLAC2D results at the borehole wall 29
Table 5.3 Undrained pore pressure at the wall: present study (Songliao) against published Tournemire simulations 31
Table 5.4 TIE against the ILE baseline, undrained, at the borehole wall . 32
Table 5.5 ILE-MC, undrained, at the borehole wall 35
Table 5.6 UBI against ILE-MC, undrained, at the borehole wall 38
Table 5.7 CANISO, undrained, at the borehole wall 41
Table 5.8 UBI against CANISO 44
Table 5.9 Hoop stress at Point B at the two simulated mud pressures 47
Table 5.10 All five constitutive models, undrained protocol, at the borehole wall 49
Table 5.11 Songliao shale (this study) against Tournemire shale, same far-field stresses and pore pressure 50

List of Figures

Figure 1 Global shale gas production by scenario to 2050 1
Figure 2 Multiple energy applications of shale formations 2
Figure 3 Typical U-shaped variation of the peak strength of shale with the bedding angle β, at three confining pressures 3
Figure 4 Illustration of stress redistribution around a vertical borehole ….5
Figure 5 Illustration of in situ stresses in different fault regimes 8
Figure 6 Schematic representation of the Lamé problem 8
Figure 7 Schematic representation of the Kirsch problem 10
Figure 8 Principle of the single plane of weakness criterion 13
Figure 9 Conceptual schematic of pore pressure and fracture gradient with depth 14
Figure 10 Petrology characteristics of oil shales and mudstones in the Songliao Basin 16
Figure 11 Songliao shale failure envelope from triaxial data 18
Figure 12 Comparison between the experimental data and the regression functions (WPM and HBm) 18
Figure 13 DONUT grid configuration in FLAC2D with Points A and B 20
Figure 14 Radial profiles of σθ and σr at Point A, ILE dry protocol, FLAC2D against the Kirsch closed-form solution 29
Figure 15 Radial profiles of σθ and σr at Point B, ILE against TIE, undrained 33
Figure 16 Tension/compression state of the wall, TIE undrained 34
Figure 17 Radial profile of σθ at Point B for ILE-MC 36
Figure 18 Zone state (plasticity) map, ILE-MC undrained 37
Figure 19 Radial profile of σθ at Point B, UBI against ILE-MC, with the UCS = 44.2 MPa reference line 39
Figure 20 Zone state map, UBI: (a) dry, pw = 0; (b) undrained, pw = 12 MPa ……40
Figure 21 Radial profile of σθ at Point B: CANISO against TIE and UBI ... 42
Figure 22 Zone state map, CANISO: (a) dry, pw = 0; (b) undrained, pw = 12 MPa 43
Figure 23 Pore fluid pressure contour map around the wellbore, undrained protocol 54

1. Introduction

1.1 The Evolving Global Energy Landscape

The global energy system is in the middle of a prolonged and uneven transition. Renewable capacity additions have accelerated in most regions, yet oil and natural gas continue to underpin electricity generation, industrial feedstocks, and transport in the medium term. Shale formations occupy a double role here: organic-rich shales are hydrocarbon reservoirs in their own right, exploited through horizontal drilling and multistage hydraulic fracturing, with continental lacustrine plays in China now joining the more established marine shales of North America as targets of active appraisal [10]; and shale intervals are also frequently the cap rock of conventional reservoirs, saline aquifers, and depleted fields now being repurposed for underground gas storage and carbon capture and sequestration, where the wellbore drilled through the cap has to stay mechanically sound for the well to be sealed and monitored safely over decades [17].

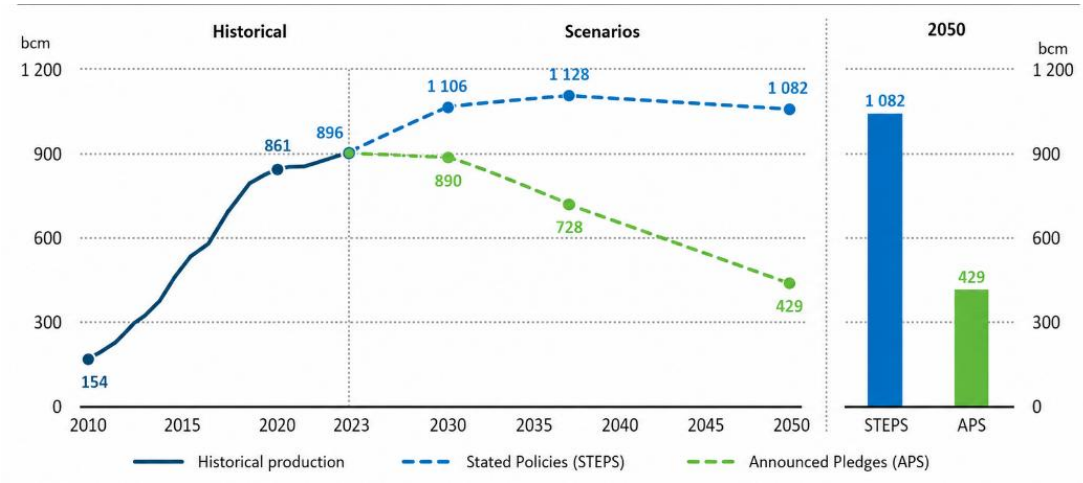


Figure 1: Global shale gas production by scenario to 2050 [13]

The scale of this role shows in the production record: enabled by horizontal drilling and multistage fracturing, shale and other tight formations now supply the large majority of United States dry natural gas output, and the United States has been the world's largest natural gas producer every year since 2011 [24]. Shale and tight gas averaged about 81 billion cubic feet per day through the first three quarters of 2024, some 79% of total U.S. dry gas production [23], and total U.S. dry gas output went on to grow more than 4% to a record-high 39 trillion cubic feet in 2025, part of a

fourth consecutive year in which the United States set an overall energy-production record [24]. Growth of this scale and staying power is why the drilling and completion engineering of shale, and within it the wellbore stability problem this chapter addresses, now carries as much economic weight as academic interest.

Drilling through shale is disproportionately expensive relative to other lithologies. Field statistics from mature basins consistently attribute a large share of non-productive time to wellbore instability in shale intervals: stuck pipe, tight hole, caving and lost circulation, forcing operators toward heavier casing strings, restricted trajectories, and abandoned acreage [2]; the penalty only grows as drilling moves into deeper, hotter, more structurally complex settings and as wellbores take on new duties as CO_2 or hydrogen storage conduits. A central reason shale is so hard to handle is that it is mechanically unlike the isotropic elastic material assumed in classical wellbore stability formulas, since its layered fabric gives it a directional strength and stiffness that no single parameter model can reproduce [26]. Recognizing and quantifying that anisotropy is the starting point for the rest of this chapter, and it motivates the numerical tools, lab tests, and failure criteria discussed next.

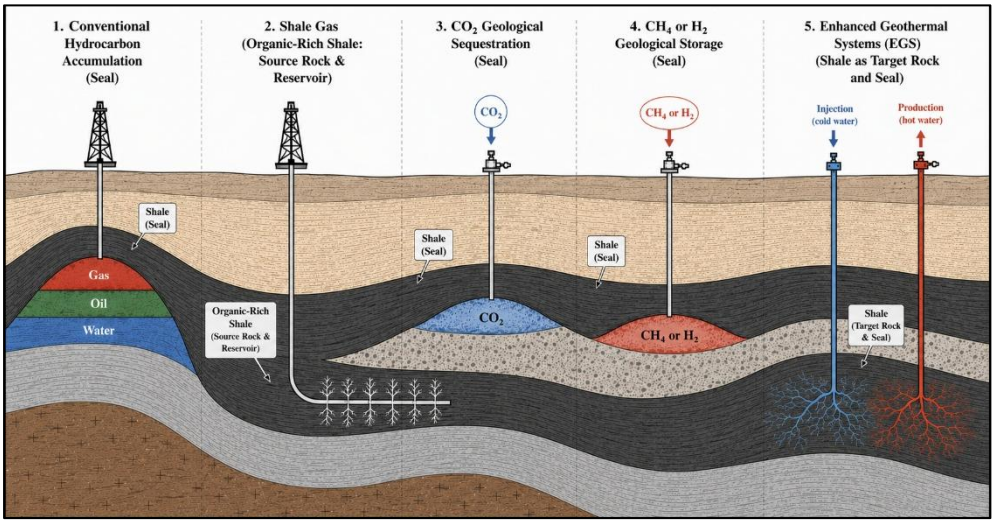


Figure 2: Schematic showing multiple energy application of shale formations. adapted from [30]

1.2 Shale as a Transversely Isotropic Rock

Shale earns the label "transversely isotropic" because it is built from parallel bedding planes: properties measured within a bedding plane are the same in every

in-plane direction, but properties measured across the bedding are not. That directionality is a direct consequence of how the rock forms; platy clay minerals settle and compact with their long axes sub-parallel to the depositional surface [4, 8] and it means shale needs five elastic constants instead of the usual two: two Young's moduli, parallel and perpendicular to bedding (E_1 and E_2), two Poisson's ratios (ν_1 and ν_2), and a shear modulus tied to planes that contain the bedding-normal axis.

This directionality is not just an elastic quirk; it shows up just as strongly in strength. Triaxial and Brazilian tests run at different bedding angles consistently trace out a U-shaped, or "saddle," strength curve: compressive strength peaks when loading runs parallel or perpendicular to bedding (0° and 90°) and bottoms out at intermediate angles, typically 45°- 60°, exactly where the load is best positioned to drive slip along the weak bedding surfaces [26, 8, 4]. Elastic modulus follows the same U-shape, and the internal friction coefficient likewise varies with direction - reported bedding-parallel/bedding-normal averages differ by roughly a fifth (about 0.72 versus 0.58), though the gap approaches a factor of two for some individual specimens [21]; acoustic emission monitoring of bedding-parallel specimens shows that the micro-cracking that leads up to failure (and how much energy it releases) is sensitive to confining pressure [25], while the failure mode itself (shear through the matrix versus slip along bedding) shifts with loading orientation relative to bedding [21, 8].

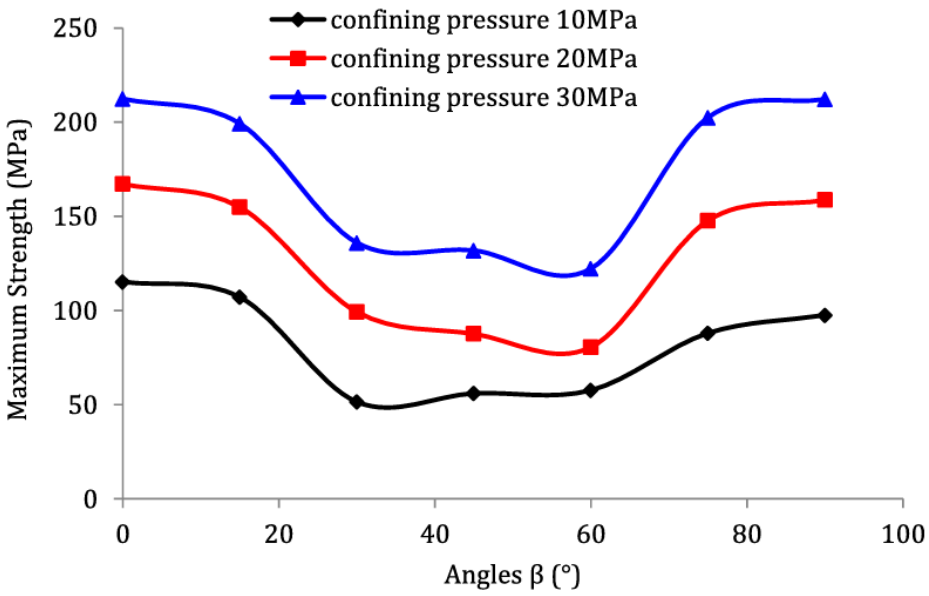


Figure 3: Typical U-shaped variation of the peak strength of shale with the bedding angle β, at three confining pressures [18]

None of this is a rounding error. Anisotropy is a first-order control on how the rock fails around an excavation, and a wellbore stability analysis that treats shale as an isotropic Mohr-Coulomb material can be badly wrong in either direction under-predicting or over-predicting the safe mud weight window, depending on well azimuth and how the bedding sits relative to the in-situ stress field [3, 19]. That is the practical case for the two anisotropic strength criteria at the heart of Chapter 2, the Weakness Plane Model and the modified Hoek-Brown criterion, and for treating anisotropy explicitly in the numerical work of Chapter 4.

1.3 Scope and Structure

This thesis investigates the stability of a wellbore drilled in transversely isotropic shale, using the Cretaceous Qingshankou shale of the Songliao Basin as the case study. The work is numerical: five constitutive models of increasing completeness are run in FLAC2D on the same grid and under the same loading, so that the effect of each physical mechanism, elastic anisotropy, matrix plasticity and bedding-plane slip, can be isolated and compared. The objective is to verify if the mud weight chosen from the conventional isotropic Mohr-Coulomb criterion is safe for this formation, and if not, which mechanism sets the collapse limit.The report is organised in six chapters.

Chapter 2 builds the analytical toolkit. It describes how drilling redistributes stress around the wellbore, sets out the effective-stress principle in its drained and undrained forms, and reviews the in-situ stress state and faulting regimes. The classical elastic solutions of Lamé and Kirsch then give the induced stresses at the wellbore wall. Four failure criteria follow, from the basic distinction between tensile and shear failure to the Mohr - Coulomb criterion, the Weakness Plane Model and the modified Hoek-Brown criterion, and the chapter closes with the mud weight window as the practical output of a stability analysis.

Chapter 3 introduces the Songliao shale. Section 3.1 summarises the depositional setting and mineralogy of the Qingshankou Formation and explains why its clay-rich, finely laminated fabric justifies a transversely isotropic treatment. Section 3.2 describes the laboratory tests that characterise the intact rock and its weak planes and presents the triaxial results and the strength regressions that supply the parameters used in the numerical models.

Chapter 4 sets up the numerical work. It introduces FLAC2D and the radial DONUT grid, the far-field stresses, pore pressure and mud pressure common to

every run, and the dry and undrained hydraulic protocols. The five constitutive models, ILE, TIE, ILE-MC, UBI and CANISO, are then presented with their parameters, and the chapter ends with the simulation plan that Chapter 5 follows.

Chapter 5 presents and discusses the results. Section 5.1 validates the isotropic elastic model against the Kirsch solution and against a published simulation of Tournemire shale. Sections 5.2 to 5.5 then add one mechanism at a time and show how each changes the stress state, the pore-pressure field and the failure pattern around the wall. Section 5.6 compares the two models that carry the bedding plane and asks which one governs. Section 5.7 turns the results into what a driller needs, the mud weight window and the sensitivity to mud pressure. Section 5.8 brings the five models together, Section 5.9 compares the Songliao shale with the previously studied Tournemire shale, and Section 5.10 states what the work contributes and where its limitations bound the conclusions.

Chapter 6 draws the conclusions and identifies the natural extensions of the work.

2. Wellbore Stability Fundamentals

2.1 Stress Redistribution During Drilling

Before a well is drilled, the rock mass at any given depth is in mechanical equilibrium under the combined action of the overburden weight, the tectonic and compaction history of the basin, and the pore fluid pressure. Drilling removes a cylindrical volume of rock and replaces it with a fluid column (the drilling mud) so that the stress that was previously carried by the excavated rock must now be redistributed onto the material immediately surrounding the new opening. Because this redistribution concentrates stress at the borehole wall rather than spreading it uniformly, the wall is systematically more likely to fail than the far-field rock, even though the far-field stresses themselves have not changed [9].

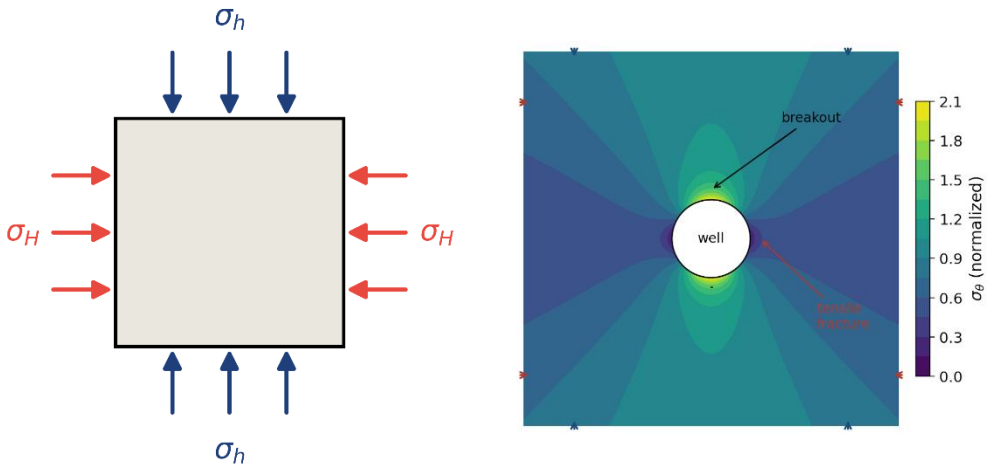


Figure 4: Illustration of stress redistribution around a vertical borehole: on the left the initial far-field stresses, on the right after removal of the rock core, breakouts form along the direction of σ_h and tensile fractures along the direction of σ_H. Adapted from [31]

The way this concentration plays out depends on the contrast between the far-field principal stresses, the inclination and azimuth of the well, and the mud pressure applied at the wall. If the mud pressure is too low relative to the concentrated compressive stress, the wall fails in shear and produces the characteristic elongated breakout visible on borehole image logs; if the mud pressure is too high relative to the least principal stress, the wall or the near-wellbore rock fails in tension, initiating a fracture that can propagate away from the

well and cause lost circulation [20]. In transversely isotropic shale, the same redistributed stress field interacts with a strength that varies with direction, so that the same magnitude of tangential stress can be safely sustained at one azimuth and cause slip along bedding at another [17]. The analytical and numerical tools developed in the rest of this chapter exist to quantify that interaction.

2.2 Effective Stress and Pore Pressure

2.2.1 Terzaghi's Principle

Shale, like most sedimentary rocks, is a porous material whose pore space is at least partially saturated with formation fluid, and its mechanical strength decreases as the pore fluid pressure increases. This behaviour is captured by the concept of effective stress, introduced for soils by Terzaghi [22] and later generalized within the framework of poroelasticity. In tensor notation the effective stress is written as

$$\sigma_{ij}' = \sigma_{ij} - \alpha u \delta_{ij} \qquad (2.1)$$

where σ_{ij}' and σ_{ij} are, respectively, the effective and the total stress tensors, μ is the pore fluid pressure, δ_{ij} is the Kronecker delta, and α is the Biot coefficient, a function of the bulk moduli of the rock skeleton, the mineral grains, and the pore fluid. Equation 2.1 in its general form assumes linear elastic behavior; for failure analysis in rock, the simpler Terzaghi definition obtained by setting $\alpha = 1$ is generally considered the most appropriate choice, and is the convention adopted throughout the strength criteria discussed later in this chapter [6]. Because the pore pressure term is isotropic, it cancels out of any principal-stress difference regardless of the value of α; under the Terzaghi convention adopted here, this means the deviatoric stress that drives shear failure can be expressed equally in terms of total or effective principal stresses: $(\sigma_1 - \sigma_3) = (\sigma_1' - \sigma_3')$.

2.2.2 Drained and Undrained Conditions

The applicability of the effective stress principle in a process such as drilling depends on whether the pore fluid has time to equilibrate with the perturbation imposed by the advancing bit and the mud column. Shale is characterized by an intrinsically low permeability, often several orders of magnitude below that of a conventional sandstone reservoir, so that the pore pressure disturbance created at the borehole wall cannot dissipate over the timescale of drilling; the rock therefore behaves, in the short term, as an undrained material [17]. Under undrained loading,

any change in the mean total stress can induces an excess pore pressure that only decays afterward, as fluid seeps away from the wellbore over time.

Numerical and analytical modelling of this phenomenon [7] show that the excess pore pressure generated immediately after drilling is not uniform around the wellbore: it is negative along the azimuth of the maximum far-field stress and positive along the azimuth of the minimum far-field stress in fault regime.

In practical terms, the zone that would otherwise appear safest from a total stress point of view can, once the pore pressure response is accounted for, be closer to failure than expected, and the reverse can also occur. Simulations carried out with FLAC2D on transversely isotropic shale confirm this pattern and show that, if this short-lived excess pore pressure is ignored, the mud pressure needed to keep the well stable in the hours right after the bit passes is understated [17]. Whether a given wellbore stability problem should be analysed under drained or undrained assumptions is therefore not a matter of convenience but a direct consequence of the permeability of the formation and the time elapsed since drilling, and both conditions are examined in the numerical study.

2.3 In Situ Stresses and Pore Pressure

The undisturbed far-field state is described by the vertical stress σ_v, the two horizontal stresses σ_{Hmax} and σ_{hmin}, and the pore pressure. Vertical equilibrium in a laterally uniform overburden fixes σ_v:

$$\sigma_v(z) = \int_0^z \rho(z) g dz \quad (2.2)$$

Where, the average density of sediments in the overburden is between (1.8 - 2.2 g/cm^3), corresponding to a gradient of roughly 20 MPa/km. The two horizontal stresses cannot be fixed by equilibrium alone: they depend on the tectonic and burial history of the basin and are instead obtained from calibrated log-based models, anchored with direct tests (LOT, FIT, mini Frac). What matters for wellbore stability is not their absolute magnitude but their size relative to σ_v and to each other, which sets the faulting regime:

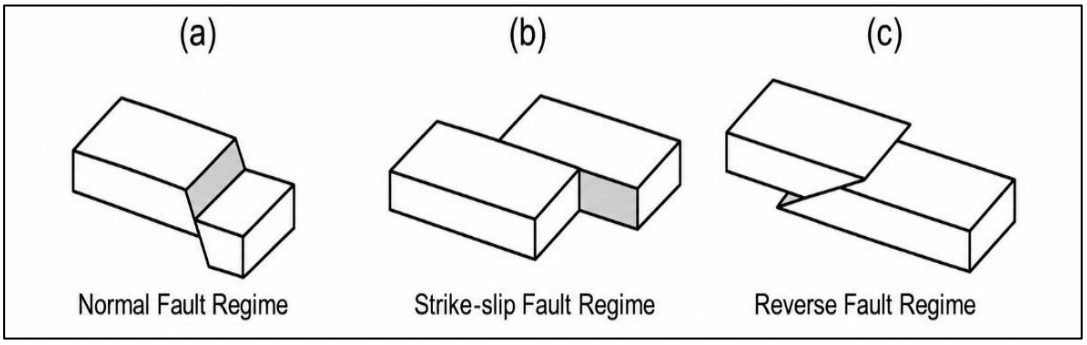


Figure 5: Illustration of in situ stresses in different fault regimes [27]

(a) Normal fault regime: $\sigma_v > \sigma_{Hmax} > \sigma_{hmin}$

(b) Strike-slip fault regime: $\sigma_{Hmax} > \sigma_v > \sigma_{hmin}$

(c) Reverse fault regime: $\sigma_{Hmax} > \sigma_{hmin} > \sigma_v$

$$R = \sigma_{Hmax} / \sigma_{hmin}$$

R is the anisotropy ratio that defines the far-field boundary condition in the FLAC2D models of Chapter 4. A normal regime favours breakout aligned with σ_{hmin}; a reverse regime favours tensile fracturing at lower mud pressure. Pore pressure follows a comparable hydrostatic baseline and is calibrated independently against MDT, LOT, and FIT data.

2.4 The Lamé Problem

The Lamé problem models a circular opening cut into an unbounded elastic solid that behaves the same way in every direction, loaded from far away by a single horizontal stress σ_h and pressurized along its own wall by mud at a pressure p_w.

Solved in cylindrical coordinates, the total stress components at a radial distance r from the well axis work out to [16]:

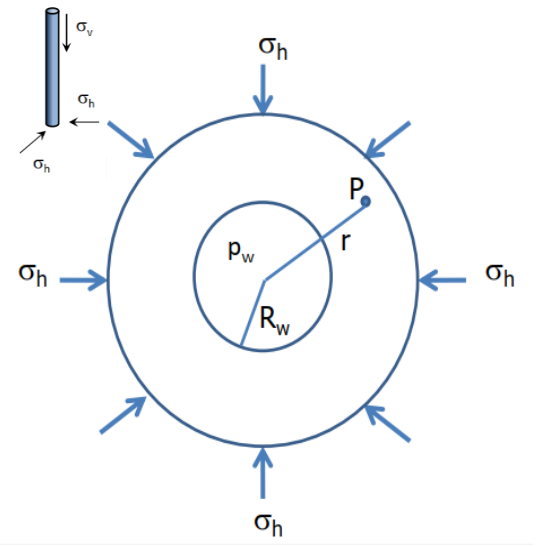


Figure 6: Schematic representation of Lamé problem

$$\sigma_r = \sigma_h\left(1 - \frac{R_w^2}{r^2}\right) + p_w\frac{R_w^2}{r^2} \quad (2.3)$$

$$\sigma_\theta = \sigma_h\left(1 + \frac{R_w^2}{r^2}\right) - p_w\frac{R_w^2}{r^2} \quad (2.4)$$

$$\sigma_{axis} = \sigma_z = \sigma_v \ , \tau_{r\theta} = \tau_{z\theta} = \tau_{zr} \quad (2.5)$$

The axial stress σ_{axis} equals the far field vertical stress σ_v at every radius, unaffected by the opening, and no shear stress is induced (Eq. 2.5). At the wall ($r = R_w$), Eq 2.3 and Eq 2.4 reduce to:

$$\sigma_r = p_w \ , \ \sigma_\theta = 2\sigma_h - p_w \quad (2.6)$$

At the wall itself, this simplifies neatly: the radial stress locks onto the mud pressure, and the hoop (tangential) stress climbs to as much as twice the magnitude of the horizontal far-field stress. That's the concentration effect behind why boreholes are so sensitive to even small changes in mud weight. The catch is that this only holds when the far-field stress is isotropic, i.e. hydrostatic; real wellbores sit under a non-hydrostatic, azimuth-dependent stress state that the axisymmetric Lamé solution can't capture, which is why the next section works through the more general Kirsch [15] solution instead.

2.5 The Kirsch Problem

Kirsch [15] solved the plane-strain problem of a circular hole of radius R_w in an infinite elastic plate under a biaxial far-field stress (σ_{max} , σ_{min}) and a uniform boundary pressure p_w . A vertical wellbore in a horizontally stressed formation fits this geometry directly, with σ_{max} and σ_{min} the two horizontal principal stresses and σ_z the far-field vertical stress treated separately along the well axis.

At the wall (r = Rw), expressed as effective stresses (Section 2.2.1), the induced stress state reduces to [6]:

$$\sigma_r' = p_w - p_f \quad (2.7a)$$

$$\sigma_\theta' = S - p_w - p_f \quad (2.7b)$$

$$\sigma_{axis}' = Sz - p_f \quad (2.7c)$$

With:

$$S = \sigma_{max} + \sigma_{min} - 2(\sigma_{max} - \sigma_{min}) \cos 2\theta \quad (2.7d)$$

$$Sz = \sigma_z - 2\nu(\sigma_{max} - \sigma_{min}) \cos 2\theta \quad (2.7e)$$

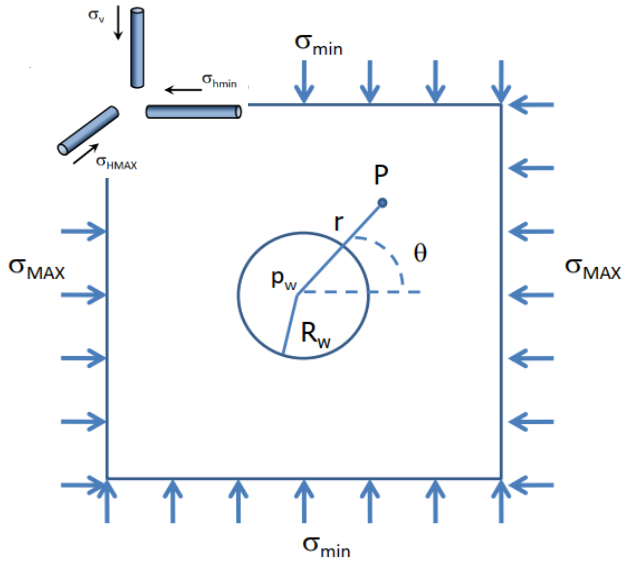


Figure 7: Schematic representation of Kirsch Problem

where θ is the azimuth measured around the wellbore wall from the direction of σ_{max}, R_w is the wellbore radius, p_w is the mud pressure, p_f is the pore fluid pressure, σ_z is the far-field vertical (axial) stress, and ν is Poisson's ratio. Equations 2.7a – 2.7b show that the tangential stress σ_θ', unlike the radial stress σ_r', is not directly proportional to the mud pressure but instead swings between a maximum and a minimum value as θ varies from 0° to 90°. Two azimuths are of particular interest, since they bound this swing and are where equations 2.7a – 2.7b are evaluated in practice:

- Point A (θ = 0°, aligned with σ_{max}): $\sigma_\theta' = 3\sigma_{min} - \sigma_{max} - p_w - p_f$ $\sigma_{axis}' = \sigma_z - 2\nu(\sigma_{max} - \sigma_{min}) - p_f$ (2.7f)
- Point B (θ = 90°, aligned with σ_{min}) : $\sigma_\theta' = 3\sigma_{max} - \sigma_{min} - p_w - p_f$ $\sigma_{axis}' = \sigma_z + 2\nu(\sigma_{max} - \sigma_{min}) - p_f$ (2.7g)

with $\sigma_r' = p_w - p_f$ at both points (Eq. 2.7a, independent of θ). Point A is where σ_θ' is least compressive (potentially tensile under strong anisotropy) and tensile failure initiates there. Point B is where σ_θ' is most compressive and shear failure is most likely. This azimuthal contrast, combined with the corresponding azimuthal variation of rock strength in an anisotropic material, is why the choice of failure criterion matters so much for shale [9, 20]. The radial stress σ′r at the wall, by contrast, is controlled directly by the difference between the applied mud pressure

and the pore pressure, which is why increasing the mud weight is the operator's primary lever for suppressing shear failure at the wall.

2.6 Failure Criteria

2.6.1 Tensile Failure

Tensile failure occurs when the effective tangential stress drops below the negative tensile strength of the rock:

$$\sigma_\theta{}' \leq -T_0 \quad (2.8)$$

Since $\sigma_\theta{}'$ is lowest at θ = 0 (Eq. 2.7f, aligned with σ_{max}), tensile failure initiates there, typically once excessive mud pressure pushes $\sigma_\theta{}'$ into tension; the resulting fracture propagates away from the well and can cause lost circulation

As a generale rule, the tensile cutoff T_0 can be obtained using the following approximation: $\frac{C_0}{T_0} = 10$

2.6.2 Shear Failure

Shear failure occurs where $\sigma_\theta{}'$ is highly compressive relative to $\sigma_r{}'$, which by Eq. 2.7d is the case at θ = 90° (aligned with σ_{min}). At the wall it appears as an elongated breakout; in an elasto-plastic model it shows as a zone of shear yielding concentrated near θ = 90° and 270° [17]. In transversely isotropic shale, shear failure can also occur by slip along a bedding-parallel weakness plane favourably oriented to the local stress state, even where the intact-rock criterion alone predicts no failure [3, 17]. Sections 2.6.3 - 2.6.5 give the strength criteria used to evaluate matrix shear failure and bedding-plane slip.

2.6.3 Mohr-Coulomb Criterion

In effective stresses, on the shear-normal plane, the Mohr-Coulomb criterion reads

$$\tau_s = c' + \sigma_n' \tan\phi'$$

equivalently, in principal stresses:

$$\sigma_1' = C_0 + N_\phi \sigma_3', \quad C_0 = \frac{2c'\cos\phi'}{(1-\sin\phi')}, \quad N_\phi = \frac{(1+\sin\phi')}{(1-\sin\phi')} \quad (2.9)$$

the uniaxial compressive strength is C_0 and the failure plane is inclined at $\beta = 45° + \frac{\phi'}{2}$ Equation 2.9 is applied with a single (c', ϕ') pair regardless of orientation; this criterion is adequate for isotropic rock but unable to capture the strength reduction along bedding, which explains the need for other criteria for anisotropic materials such as shale. Both anisotropic criteria below are built on this same linear form.

2.6.4 Weakness Plane Model (WPM)

The Weakness Plane Model [14] treats bedding as a plane of weakness with its own Coulomb strength (c'_w, ϕ'_w), independent of the matrix (c', ϕ'). Slip occurs when [6]:

$$(\sigma'_1 - \sigma'_3)_{slip} = \frac{2(c'_w + \sigma'_3 \tan\phi'_w)}{\left(1 - \frac{\tan\phi'_w}{\tan\beta_w}\right)\sin 2\beta} \quad (2.10)$$

It predicts the minimum strength at $\beta_w = 45° + \frac{\phi'_w}{2}$. β_w near 0° or 90° slip cannot occur, and the Mohr-Coulomb criterion governs instead, so at each azimuth θ we evaluate both criteria and the lower strength one is retained.

2.6.5 Modified Hoek-Brown Criterion

The Hoek-Brown criterion [11], adapted here to transversely isotropic rock [5, 6], replaces the WPM's matrix/plane split with a single continuous function of β_w:

$$\sigma'_1 = \sigma'_3 + (mC_0\sigma'_3 + sC_0^2)^{0,5} \quad (2.11)$$

Where m and s are dimensionless strength parameters varying with rock type.

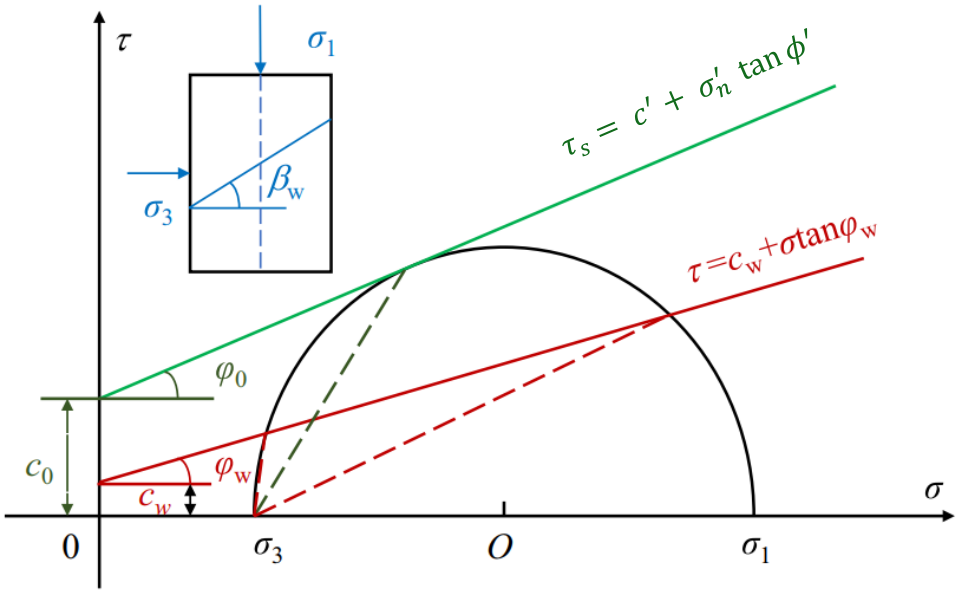


Figure 8: Principle of single plane of weakness criterion [19]

2.7 Mud Pressure and Mud Weight Window

The practical output of a wellbore stability analysis is the mud weight window: the range of mud pressures, usually expressed as an equivalent mud density, within which the well can be safely drilled. The lower bound of the window is set by the collapse (or breakout) pressure, the minimum mud pressure that keeps the tangential stress at the wall below the shear strength predicted by the chosen failure criterion; the upper bound is set by the fracture (or lost circulation) pressure, the maximum mud pressure that can be applied before the tangential stress becomes tensile and exceeds the tensile strength of the rock, or before an existing fracture is reopened. Because the tangential stress varies with azimuth (Eq 2.7d) and, in anisotropic shale, the strength varies with the orientation of bedding relative to that azimuth, both bounds of the window are themselves functions of wellbore azimuth and inclination, not single numbers.

In transversely isotropic shale specifically, the mud weight window must additionally be checked against the possibility of bedding-plane slip at azimuths and inclinations where the intact-rock criterion alone would appear satisfied. Numerical simulations with FLAC2D confirm that increasing mud pressure systematically shrinks the zone of matrix and bedding-plane failure predicted around the wellbore, but that the required mud pressure to suppress bedding plane slip can differ substantially in either direction from the pressure required to suppress

matrix shear failure, depending on the chosen constitutive model and on whether dry or undrained conditions are assumed [17].

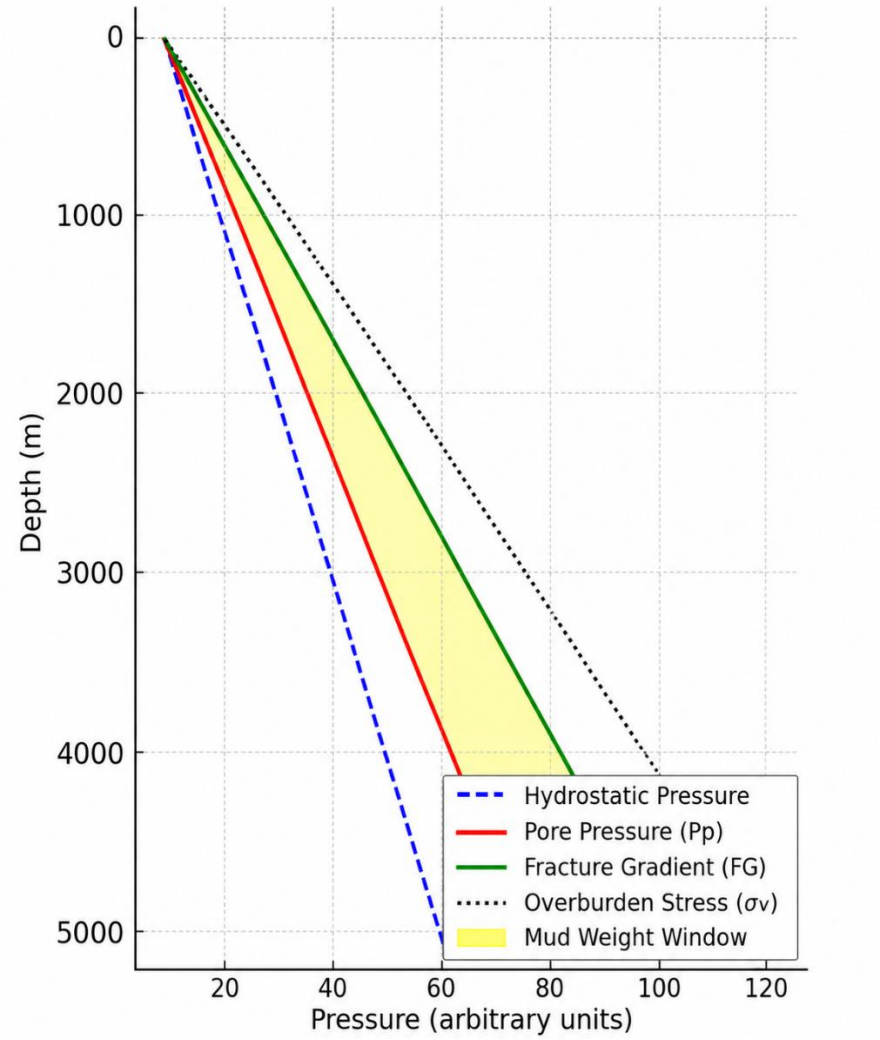


Figure 9: Conceptual schematic of pore pressure and fracture gradient with depth. Hydrostatic pressure follows the normal compaction trend, while overpressured formations deviate from it [28]

3. Songliao shale: geological and geomechanical context

3.1 Depositional settings:

The data set selected for the numerical work are coming from the oil-shale-bearing levels of the Qingshankou Formation (K2qn1) in the Songliao Basin, north-eastern China, deposited in a semi- deep to deep-lake facies [12]. The oil shale is light brown with horizontal, sub-millimeter lamination, while the interbedded mudstone is dark grey to greyish-black with a massive structure and contains thin dolomite layers and ostracod/Estheria fossils indicating a shallow, unstable-water interval; across the 15 samples classified as oil shale (oil yield ≥ 3.5%), oil yield ranges 3.6 -7.3%, TOC 2.6 - 8.7%, and total sulfur 0.6 - 4.1%, consistent with deposition under a warm-humid climate in a saline, strongly reducing lake [12].

Table 3.1 summarizes the average whole-rock mineralogy of the formation's oil shale and mudstone from X-ray diffraction analysis [12]. The high clay content is linked to the abundance of organic matter, while the syngenetic pyrite content indicates the oxygen-deficient bottom-water conditions typical of oil-shale deposition [12].

Table 3.1: Average whole-rock mineralogy of the Qingshankou (K2qn1) oil shale and mudstone, southern Songliao Basin [12]

Component	**Content (%)**
Clay minerals (total)	56.8
Quartz	24.0
Plagioclase	12.4
Pyrite	3.4
Dolomite	2.4
Alkali feldspar	0.6
Calcite	0.4

These mineralogical and textural characteristics translate directly into the geomechanical behaviour this thesis sets out to capture. A clay fraction above half the rock volume, arranged in millimeter-scale horizontal bedding, is the physical basis for treating the Songliao shale as transversely isotropic in the first place: it

produces the distinct in-plane and cross-plane elastic moduli carried into the TIE model, the weak bedding planes exploited by the WPM and CANISO models, and the strength anisotropy quantified by the Hoek-Brown constants of Section 2.6.5.

The dolomite laminae and syngenetic pyrite, in turn, record the diagenetic and redox history that governs cementation and, through it, the matrix cohesion and friction angle recovered from laboratory testing (Section 3.2).

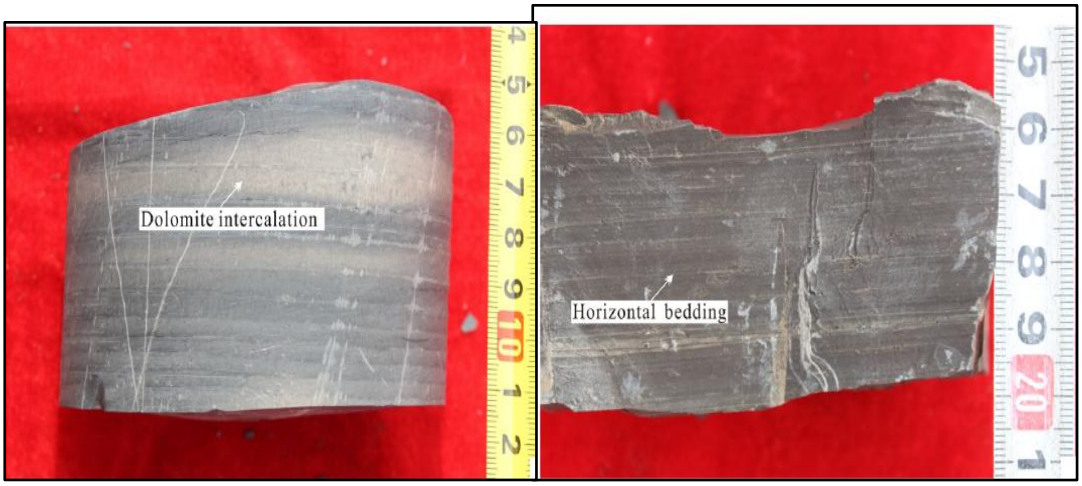


Figure 10: Petrology characteristics of oil shales and mudstones in the Songliao Basin [12].

Triaxial, uniaxial test results provide the matrix and weak-plane strength parameters carried through Chapter 2 and into the FLAC2D constitutive models.

3.2 Interpretation of laboratory tests:

Before any failure criterion can be applied, the intact rock and its weak planes must be characterized in the laboratory, through three complementary tests on core specimens cut at controlled angles between the loading axis and the bedding normal.

The uniaxial compression test loads an unconfined cylindrical specimen along its axis until it fails. It is the simplest test to run, and it gives a first estimate of the unconfined compressive strength (UCS), together with, from the linear part of the stress-strain curve, the Young's moduli E1 and E2 and the Poisson's ratios at each bedding angle.

The triaxial compression test addresses that limitation: the same kind of specimen is loaded axially while a confining pressure acts on its lateral surface, reproducing more realistic in-situ conditions. Repeating the test at several confining pressures gives a series of failure points that, once fitted, yield the matrix cohesion c′ and friction angle ϕ′; repeating it across bedding angles additionally yields the weak-plane parameters c'_w and ϕ'_w and the instantaneous Hoek-Brown constants σ_{c,β_w}, m_{β_w} used in Section 2.6.

Because rock is weak in tension and a direct pull test is hard to run reliably, tensile strength is generally measured indirectly with the Brazilian disc test: a thin disc is compressed diametrically until it splits along the loading plane. The load at failure converts into the indirect tensile strength T_0 and its variation with bedding orientation, which sets the fracture (upper) bound of the mud weight window in Section 2.7. In our case, Brazilian test was not conducted, and T_0 was estimated using the approximation used in section 2.6.1 .

Numerical and analytical analyses of wellbore instability need the mechanical parameters reported in Table 3.2. For these analyses, the results of triaxial tests carried out by Li et al: Study on the mechanism of anisotropic wellbore instability in continental shale in Songliao Basin [32] and Li et al: Study of wellbore instability and collapse mechanism for a layered continental shale oil horizontal well [33] were interpreted.

Figure 11 shows the measured triaxial failure envelopes (σ'_1 versus tσ'_3) of the Songliao shale at each tested weakness-plane inclination, confirming that the axial strength is lowest at β_w = 60° and highest at β_w = 90° across all confining pressures. Figure 12 shows the regression of the uniaxial compressive strength σ_c against β_w, with the WPM and H&Bm functions (Sections 2.6.4 - 2.6.5) fitted to this experimental data; both functions capture the pronounced strength minimum near $\beta_w \approx$ 55° - 60° identified in Figure 12.

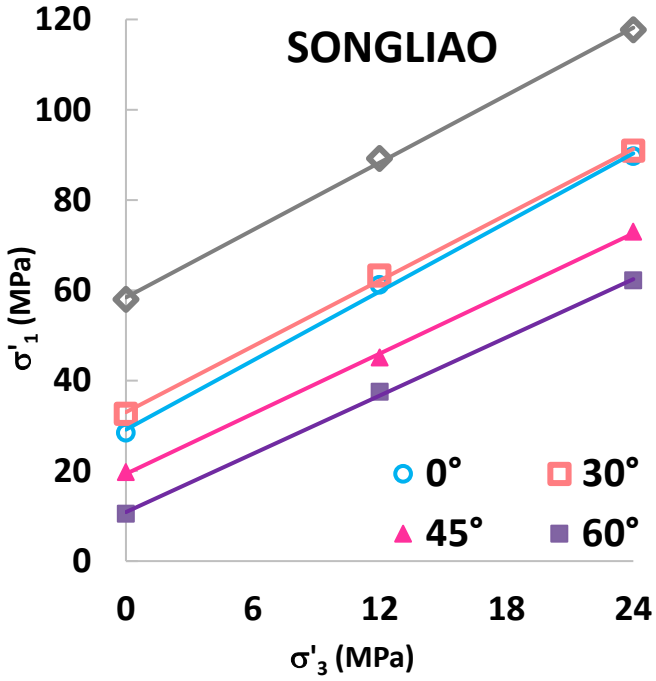


Figure 11: Songliao shale failure envelope from triaxial data [29]

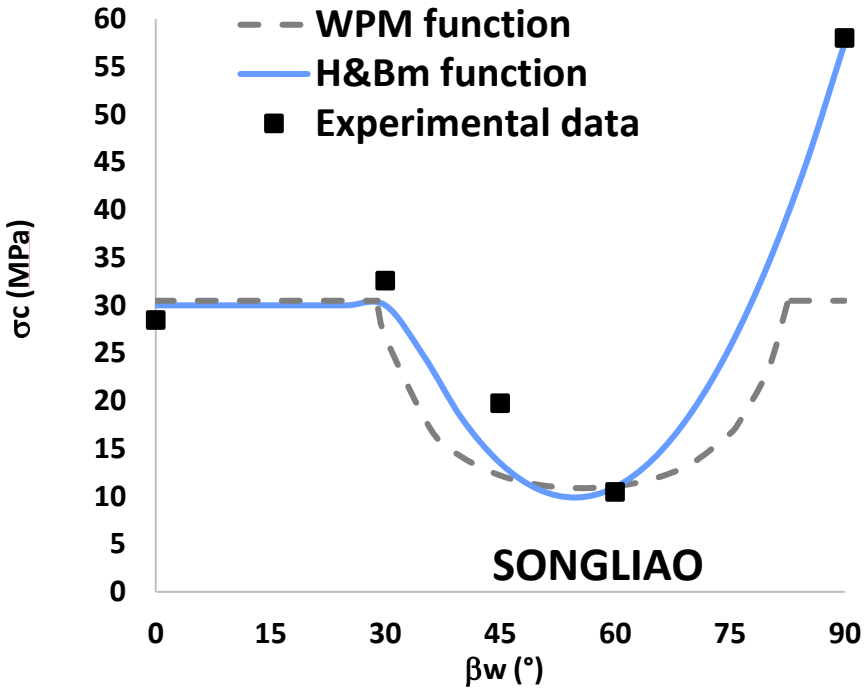


Figure 12: Comparison between the experimental data regressions functions [29]

4. Numerical Modeling with FLAC2D

4.1 Introduction to FLAC2D

FLAC2D (Fast Lagrangian Analysis of Continua) is a two-dimensional explicit finite-difference code for geomechanical analysis, widely used in petroleum and mining geomechanics because its explicit time-marching scheme handles strongly non-linear, path-dependent constitutive behaviour including the strain-softening, anisotropic plasticity models required for bedded shale, without the convergence difficulties that can affect implicit solvers under similar conditions. For wellbore stability problems, the domain is typically discretized as a radial grid centred on the borehole axis (implemented in FLAC2D through the built-in "DONUT" grid generator), which concentrates zones near the wall where stress gradients are steepest and allows the far-field boundary to be placed at a distance large enough to approximate an infinite medium [6, 17]. Once the far-field stresses, pore pressure, and mud pressure are imposed as boundary conditions, the code marches the model to mechanical equilibrium and reports, at every zone, the stress state, the pore pressure, and whether the material is behaving elastically, has yielded in the matrix, or has slipped along an embedded weakness plane.

The relevance of FLAC2D to the present chapter is that it allows the analytical criteria of Chapter 2 the Kirsch stress solution and the WPM/HBm strength criteria to be embedded within a fully coupled elasto-plastic and, where required, poromechanical simulation, so that effects that the closed-form Kirsch solution cannot capture on its own (stress redistribution after yielding, the spatial extent of the failed zone, the transient pore-pressure response under undrained conditions) can be examined directly. Sections 4.2 to 4.4 describe, respectively, the geometry and boundary conditions of the model, the constitutive models available for representing anisotropic shale in FLAC2D, and the comparison between dry and undrained simulation conditions.

4.2 Model Setup: DONUT Grid and Boundary Conditions

All the numerical simulations in this thesis share the same geometry, grid, boundary conditions, and in-situ stresses; only the material block and the hydraulic setup change from one constitutive model to the next, so any difference in the results can be attributed to the constitutive law itself and not to the setup. The model is built on a radial "DONUT" grid centred on the wellbore axis, introduced in Section 4.1:

60 zones in the radial direction and 60 in the circumferential direction, with a geometric ratio of 1.1 that concentrates the zones near the wellbore wall, where the stress and pore-pressure gradients are steepest. The wellbore radius is R_w = 0.5 m, and the outer boundary is placed at 20 m (R_w x 40) far enough that the imposed far-field stresses are recovered undisturbed.

The far-field stresses applied at the outer boundary are $\sigma_{Hmax} = 30$ MPa MPa and $\sigma_{hmin} = 20$ MPa in the horizontal plane, and σ_v = 25 MPa out-of-plane, giving a stress anisotropy ratio R = 1.5.

The two reference points introduced with the Kirsch solution in Section 2.5 are tracked around the wellbore wall: Point A (θ = 0°), aligned with σ_{Hmax}, where the tangential stress is minimum, and Point B (θ = 90°), aligned with σ_{hmin}, where the tangential stress is maximum and failure is expected to start first. Horizontal weak planes are embedded in the model, so the angle β_w between the weak-plane normal and the local principal stress direction varies continuously with azimuth θ around the wellbore wall, exactly as anticipated in the description of the WPM in Section 2.6.4.

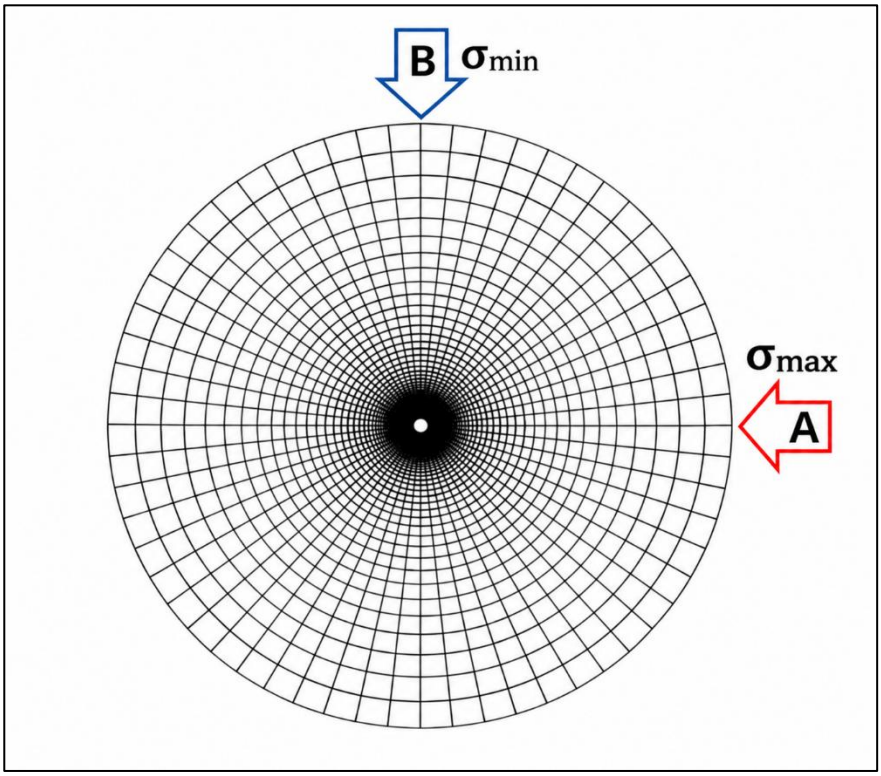


Figure 13: DONUT grid configuration on FLAD2D with points A & B

Boundary and loading conditions are applied in two stages. First, the far-field stresses are imposed at the outer boundary, and the model is brought to equilibrium with the wellbore not yet excavated, replicating the in-situ state described in Section 2.3. Second, the material inside the wellbore radius is removed and a uniform mud pressure pw is applied at the new internal boundary: 0 MPa in the dry cases (open hole) and 12 MPa in the undrained cases, with an initial pore pressure pf of 11 MPa meaning the well is drilled slightly overbalanced. At the solver level, the dry condition runs as a purely mechanical grid, flagged with an extra per-zone memory allocation (extra=5); the undrained condition additionally activates FLAC2D's coupled groundwater-flow module (gwflow extra=5) on the same grid, so pore pressure is solved together with the mechanical equilibrium under Skempton coupling (Table 4.2, Section 4.3).

Because the same grid and boundary sequence are reused, unchanged, for every constitutive model, the mesh resolution and boundary placement are first verified against the Kirsch analytical solution of Section 2.5 using the isotropic linear elastic model (ILE) alone, under both the dry and undrained protocols. Only once this baseline reproduces the closed-form elastic solution is the same grid and boundary configuration carried forward, without modification, to the remaining four models (TIE, ILE-MC, UBI, CANISO). Table 4.1 summarizes the common parameters of the model setup; the material, elastic, and joint parameters specific to each constitutive model are introduced in Section 4.3.

Table 4.1: Common parameters of the numerical model setup

Parameter	**Value**	**Meaning**
Wellbore radius	R_w = 0.5 m	/
Outer boundary	20 m (40 × R_w)	Far-field stresses unperturbed
Grid	60 × 60 zones	Radial × circumferential
Geometric ratio	1.1	Mesh refinement near the wall
σ_{Hmax}	30 MPa	Maximum horizontal stress
σ_{hmin}	20 MPa	Minimum horizontal stress
σ_v	25 MPa	Vertical (Overburden) stress
p_f (initial, undrained)	11 MPa	Pore pressure
p_w (undrained)	12 MPa	Mud pressure, overbalanced

4.3 Constitutive Models

As anticipated in Section 2.6, the failure criteria developed analytically in Chapter 2 find their numerical implementation here. FLAC2D offers several constitutive models, and five of them are used in this thesis, presented below from the simplest to the most complete: the isotropic linear elastic model (ILE), the transversely isotropic elastic model (TIE), the isotropic Mohr-Coulomb model (ILE-MC), the Ubiquitous Joint model (UBI), and the CANISO model coupling transverse isotropy with direct weak-plane slip. Each model adds one new physical mechanism on top of the previous one - elastic anisotropy, matrix plasticity, weak-plane slip - so its effect can be isolated by direct comparison. The ILE model alone is run under both the dry and undrained hydraulic protocols of Table 4.2, providing the baseline check of the grid and boundary-condition configuration described in Section 4.2 before any further physics is introduced; the remaining four models (TIE, ILE-MC, UBI, CANISO) are then run under the undrained protocol only, using material parameters derived from the laboratory tests of Section 3.2, so that differences between models are attributable to the constitutive law alone.

Table 4.2: Hydraulic protocol and grid configuration

Condition	FLAC2D config	Water bulk modulus Kw	Initial pore pressure pf	Well (mud) pressure pw	Applied to
Dry	extra = 5	no fluid	0 MPa	0 MPa (open hole)	ILE only
Undrained	gwflow extra = 5	2 GPa (Skempton coupling)	11 MPa	12 MPa (overbalanced)	ILE, TIE, ILE-MC, UBI, CANISO

4.3.1 ILE - Isotropic Linear Elastic

This is the simplest model in the hierarchy: the rock is isotropic and elastic and never fails - the stress-strain relation stays linear no matter how high the load gets, with Hooke's law written in terms of two independent elastic constants, the bulk modulus K and the shear modulus G (Table 4.3). Because an analytical solution exists for this case, ILE is used to validate the grid against the Kirsch solution of Section 2.5 and to provide the reference elastic stress distribution around the wellbore. As the first model run, ILE also serves as the baseline check of the DONUT grid and boundary condition configuration of Section 4.2, under both the

dry and undrained protocols; the same grid is then reused, unchanged, for the remaining four models.

Table 4.3: ILE material parameters [32,33]

Parameter	Symbol	Value
Density	ρ	2500 kg/m^3
Bulk modulus	K	6.6 GPa
Shear modulus	G	4 GPa

4.3.2 TIE - Transversely Isotropic Elastic

Same as ILE, but with elastic anisotropy: the rock is stiffer along the bedding (E_1) than across it (E_2), using the five elastic constants introduced in Section 1.2 (Table 4.4), which give an anisotropy ratio $E_1/E_2 = 2.04$. There is still no failure criterion. The softer direction deforms more under the same load, so the stress redistributes to keep equilibrium: higher tangential stresses are expected at the wall, especially at Point B, meaning the anisotropy alone, before any failure is considered, already makes conditions there more severe than in ILE. Unlike ILE, TIE is run under the undrained protocol only (Table 4.2), on the same grid and boundary conditions already validated with ILE, so that any difference between the two models is attributable to elastic anisotropy alone.

Table 4.4: TIE elastic parameters [32,33]

Parameter	Symbol	Value
Bedding angle	δ	0°
Young's modulus, parallel to bedding	E_1	10 GPa
Young's modulus, perpendicular to bedding	E_2	4.9 GPa
Out-of-plane shear modulus	G_{12}	2.51 GPa
In-plane Poisson's ratio	ν_{12}	0.18
Out-of-plane Poisson's ratio	ν_{23}	0.23

4.3.3 ILE-MC - Isotropic Mohr-Coulomb

The isotropic elastic model combined with the Mohr-Coulomb yield criterion of Section 2.6.3 for the rock matrix (Table 4.5). Below the yield surface the rock behaves elastically; once the criterion is reached, plastic deformation sets in and the excess stress is redistributed to the neighbouring zones the first model in the hierarchy to produce irreversible deformation. At Point B the elastic stress is expected to exceed the strength of the rock, so a yielded zone should form at the wall, with the stress peak moving away from it into the formation and forming a stress arch: the classical breakout pattern. Weak planes are ignored in this model, so it isolates the case where only matrix failure is considered. The matrix strength parameters give a uniaxial compressive strength C_0 = 44.2 MPa.

Table 4.5: ILE-MC material parameters [32,33]

Parameter	**Symbol**	**Value**
Bulk modulus	K	6.6 GPa
Shear modulus	G	4.0 GPa
Density	ρ	2500 kg/m3
Cohesion	c′	13.8 MPa
Friction angle	ϕ′	26°
Tensile cutoff	T_0	4.4 MPa
Dilation angle	ψ	0°

The tensile cutoff used in the ILE-MC model (T_0 = 4.4 MPa, Table 4.5) is obtained using the approximation in section 2.6.1.

4.3.4 UBI - Ubiquitous Joint

The numerical counterpart of the WPM presented in Section 2.6.4: failure can occur in the matrix (Mohr-Coulomb), along the weak planes (slip criterion), or both (Table 4.6). FLAC2D checks the matrix first, applies the plastic correction, then re-evaluates the weak planes against the corrected stress, so matrix plasticity can influence the slip, something the analytical WPM cannot do. Because the weak-plane friction angle is markedly lower than the matrix (21° against 26°, with cohesion at about 27% of the matrix value), the planes are expected to slip more easily and act as an additional stress-release mechanism: compared to ILE-MC, a

lower stress peak is expected around the wellbore, because part of the load is dissipated by slipping along the bedding instead of accumulating in the arch , although Section 5.4 shows this holds only away from the wall itself, where the arch would otherwise have relieved the wall directly.

Table 4.6: UBI/CANISO joint (weak plane) parameters [32,33]

Parameter	Symbol	Value
Joint orientation	/	0°
Joint cohesion	c'_w	3.7 MPa (≈27% of matrix)
Joint friction angle	ϕ'_w	21° (< matrix 26°)
Joint tensile cutoff	T_{0w}	3.0 MPa
Joint dilation angle	ψ_w	0°

4.3.5 CANISO - Transversely Isotropic Elastic with Weak-Plane Slip

Combines the TIE elastic anisotropy (Table 4.4) with the weak-plane parameters of UBI (Table 4.6), applied on the same horizontal bedding plane. The elasticity is transversely isotropic, and failure occurs only along the weak planes: the matrix itself carries no cohesion, friction, or tensile cutoff and cannot yield in this model. CANISO also checks slip directly on the anisotropic (TIE) stress state, without any prior matrix correction unlike UBI. Because the TIE background already amplifies the stress at the wall, and no matrix plasticity is there to soften it, the near-wall stress is expected to be the highest of the five models, with failure concentrated along the bedding planes. Comparing UBI and CANISO under the same conditions isolates the effect of elastic anisotropy on the failure pattern.

Table 4.7: Summary of the five constitutive models used in this thesis

Model	Elastic behaviour	Rock matrix failure	Weak-plane failure
ILE	Isotropic	/	/
TIE	Transversely isotropic	/	/
ILE-MC	Isotropic	Mohr-Coulomb	/
UBI	Isotropic	Mohr-Coulomb	Slip / tension
CANISO	Transversely isotropic	/	Slip / tension

The five models are executed in this fixed order: ILE, TIE, ILE-MC, UBI, CANISO. ILE alone is run under both the dry and undrained hydraulic protocols of Table 4.2 to validate the grid and boundary-condition setup of Section 4.2; the remaining four models are then run under the undrained protocol only.

4.4 Simulation Plan

The numerical work proceeds in two stages, following directly from the grid validation and model hierarchy set out in Sections 4.2 and 4.3. In the first stage, the ILE model is run under both the dry ($p_f = 0$) and undrained ($p_f = 11$ MPa, $p_w = 12$ MPa) hydraulic protocols of Table 4.2, and its predicted stress and, under the undrained protocol, pore-pressure field is compared against the closed-form Kirsch solution of Section 2.5 at Points A and B. This comparison serves as the baseline check of the DONUT grid resolution and boundary-condition configuration before any additional physics is introduced. In the second stage, once the ILE baseline is validated, the same grid and boundary conditions are reused, unchanged, to run the TIE, ILE-MC, UBI, and CANISO models under the undrained protocol only, so that the resulting stress, pore pressure, and where a failure criterion is defined plastic-yield and weak plane slip fields can be compared against the ILE baseline and against one another, isolating in turn the effect of elastic anisotropy (TIE), matrix plasticity (ILE-MC), weak-plane slip (UBI), and the combination of anisotropic elasticity with weak-plane slip (CANISO).

For each elasto-plastic model, the induced stress field around the wellbore wall is examined against the matrix Mohr-Coulomb criterion and, where a weak plane is present, the WPM criterion of Section 2.6, for both compressive (breakout) and tensile (fracture) failure exceedance, together with the sensitivity of the resulting failure extent to mud pressure. Under the undrained protocol, the excess pore pressure generated at the wellbore wall is tracked following the pattern anticipated in Section 2.2.2 negative at Point A and positive at Point B, and its influence on the effective stress and failure state is assessed alongside the purely mechanical response. The resulting stress, pore pressure, and failure predictions for all five models, together with their validation against the Kirsch solution and, where relevant, their comparison against the broader literature are presented in the next chapter.

5. Results and Discussion

This chapter presents the results of the two-stage simulation plan described in Section 4.4. Section 5.1 checks that the DONUT grid and boundary conditions from Section 4.2 reproduce the closed-form elastic solution, using the isotropic linear elastic model under both the dry and undrained protocols of Table 4.2; this is the only place in the thesis where both protocols are compared. Sections 5.2 – 5.5 give the undrained results for TIE, ILE-MC, UBI and CANISO, each one adding a single new mechanism: elastic anisotropy, matrix plasticity, bedding-plane slip, and finally both anisotropies together so its effect can be isolated. Section 5.6 puts UBI and CANISO side by side, since they are the only two models carrying the weak plane. Section 5.7 turns the numerical output into the mud weight window that Section 2.7 set up as the practical goal of the whole analysis and works through what a drilling engineer could do with it. Sections 5.8 and 5.9 pull the five models together and compare them with published results on other shales, and Section 5.10 sums up what this work adds and where its limits are.

Point A ($\theta = 0°$, aligned with σ_{Hmax}) and Point B ($\theta = 90°$, aligned with σ_{hmin}), introduced in Section 4.2, remain the two azimuths used to read off results throughout the chapter. Tangential stress is lowest at A, where tensile failure is expected, and highest at B, where shear failure starts. Effective stresses are computed from Eq. 2.1 with $\alpha = 1$ throughout.

5.1 Validation of the Numerical Model

Before drawing any conclusion about constitutive behaviour, the mesh needs to be shown to solve the problem it was set up for. The isotropic linear elastic model is the right tool for that check: it has no failure criterion, so its response is fixed entirely by the Kirsch solution of Section 2.5, and any gap between FLAC2D and the closed form has to come from the discretisation or the boundary conditions, not the material law. Following Table 4.2, ILE is run under both hydraulic protocols: dry, to isolate the mechanical response on its own, and undrained, to add the poro elastic coupling on the same grid. Once both checks pass, the dry protocol has done its job and will not be our focus in Sections 5.2 - 5.5.

5.1.1 Dry Protocol

With pf = pw = 0, effective and total stresses are the same (Eq. 2.1, α = 1), and Eqs. 2.7 f-g reduce to $\sigma_\theta = 3\sigma_{hmin} - \sigma_{Hmax}$ at Point A and $\sigma_\theta = 3\sigma_{Hmax} - \sigma_{hmin}$ at Point B. That gives analytical targets of 30 MPa and 70 MPa.

Table 5.1: ILE, dry protocol: FLAC2D results at the borehole wall against the Kirsch solution.

Quantity	**Kirsch target**	**FLAC2D**	**Error**
σ_θ at Point A (θ = 0°)	30.00 MPa	30.26 MPa	+ 0.87%
σ_θ at Point B (θ = 90°)	70.00 MPa	69.01 MPa	- 1.41%
σ_r at the wall (both points)	0 MPa	= 0.3 MPa	/
Far-field σ_{Hmax}	30.00 MPa	30.00 MPa	0.00%
Far-field σ_{hmin}	20.00 MPa	20.05 MPa	+ 0.25%

This is close enough to move forward. Errors stay below 1.5% at the two wall points and below 0.9% in the far field, which is what a 60×60 grid with a geometric ratio of 1.1 should deliver, and confirms that the mesh resolves the near-wall gradient while the outer boundary at 40 R_w is far enough away to leave the far field undisturbed. The one thing worth explaining is the small non-zero radial stress at the wall = 0.3 MPa against a target of exactly zero. This isn't a boundary-condition error; FLAC2D reports stresses at zone centroids, so the value plotted “at the wall” is really sampled half a zone width inside it, where σ_r has already started rising from zero. That same centroid offset is why the Point B hoop stress comes in slightly below the analytical maximum and the Point A value sits slightly above the minimum: centroid sampling pulls both extremes a little toward the interior solution. It's a known, quantifiable feature of the discretisation, not a defect, and at this size it doesn't change any conclusion in the rest of the chapter. Figure 14 plots the two curves directly at Point A.

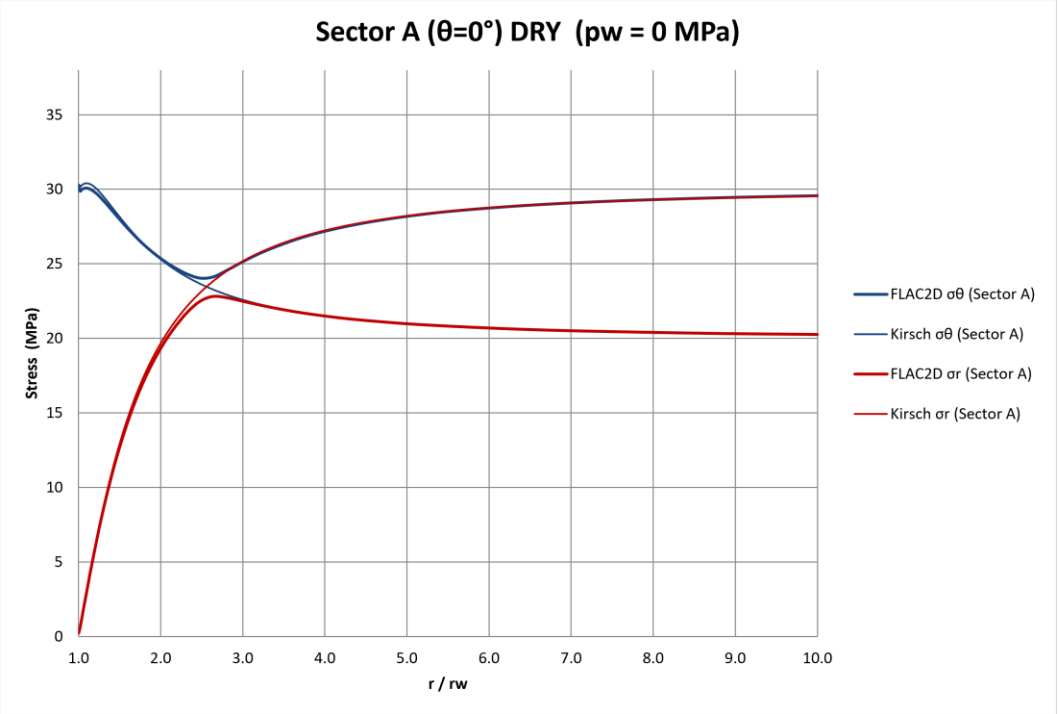


Figure 14: Radial profiles of σ_θ (blue) and σ_r (red) from the wall to the far field at Point A, ILE dry protocol (pw = 0 MPa), FLAC2D against the Kirsch closed-form solution.

5.1.2 Undrained Protocol

Under the undrained protocol the coupled groundwater-flow module (gwflow, Kw = 2 GPa) runs on the same grid, so the change in mean total stress caused by excavating the wellbore is shared between the solid skeleton and the pore fluid rather than carried entirely by the skeleton. Section 2.2.2 anticipated this mechanism qualitatively; Table 5.2 shows it in the numbers.

Table 5.2: ILE, undrained protocol (pf = 11 MPa, pw = 12 MPa): FLAC2D results at the borehole wall.

Quantity	**Point A (θ = 0°)**	**Point B (θ = 90°)**
Total hoop stress σ_θ	18.40 MPa	57.22 MPa
Total radial stress σ_r	12 MPa	12 MPa
Pore pressure pf	5.94 MPa	16.16 MPa
Effective hoop stress σ_θ' (Eq. 2.7b)	12.46 MPa	41.06 MPa

Quantity	Point A (θ = 0°)	Point B (θ = 90°)
Effective radial stress σ_r' (Eq. 2.7a)	6.06 MPa	- 4.16 MPa

Far field pore pressure returns to 11.00 MPa at both azimuths, and the far field total stresses recover the imposed 30/20 MPa to within 0.3% so the fluid boundary condition isn't disturbing the mechanical one.

The total hoop stresses match the analytical values from substituting pw = 12 MPa into Eq. 2.7f - g (18.00 and 58.00 MPa) to within +2.2% and -1.3%, so the mud-pressure boundary condition and the elastic redistribution are correct on their own, independent of the fluid coupling. The pore pressure row is where the new physics shows up: pf drops below its far-field value at Point A and rises above it at Point B; the Skempton dipole from Section 2.2.2. The sign at each point comes straight out of the change in mean stress. Taking the in-plane mean stress at the wall as (σ_θ + σ_r)/2, Point A drops from a far field 25 MPa to 15.2 MPa, a net unloading that pulls pore pressure down, while Point B rises to 34.6 MPa, a net loading that pushes it up. Reproducing both the sign and roughly the size of this asymmetry, on a grid whose mechanical behaviour was already checked in Section 5.1.1, is what the undrained validation rests on.

Two things follow from this that matter for the rest of the chapter, and both are already in Table 5.2. First, what happens if you ignore the dipole. Plugging the uniform far field pf = 11 MPa into Eq. 2.7b gives $\sigma_\theta' \approx 7$ MPa at Point A and $\sigma_\theta' \approx 47$ MPa at Point B. Comparing these with the coupled values shows the two azimuths move in opposite directions: at Point A the coupled effective stress is higher than the uniform pf estimate (12.46 vs. 7 MPa), so ignoring the dipole overstates the tensile margin there; at Point B the azimuth that controls shear failure in every model in this chapter , the coupled value is lower (41.06 vs. 47 MPa), so ignoring the dipole understates how close the wall actually is to yielding. This isn't specific to this one run; it's the same mechanism behind Liu et al [17] conclusion that neglecting the excess pore pressure generated right after drilling underestimates the mud pressure needed for stability, and Table 5.2 reproduces it independently.

The second consequence is smaller in scope but less obvious. Eq. 2.7a gives the effective radial stress at the wall as σ_r' = pw - pf. Using the uniform far-field pore pressure, this stays a comfortable +1 MPa everywhere. Using the locally computed pore pressure instead, it becomes 12 – 16.16 = - 4.16 MPa at Point B the wall is in effective radial tension, even though the total radial stress there is compressive and pinned at the mud pressure. Once the undrained overpressure exceeds the mud pressure, the mud can no longer hold the pore fluid in, and the rock skeleton at the

wall is effectively being pulled apart by its own fluid. That's a plausible mechanism for near-wellbore microcracking and spalling, on top of the hoop stress driven breakout that dominates the rest of the chapter, and Section 5.2 shows it directly in the FLAC2D tension/compression output. It's also the mechanism Section 5.5 needs to explain the tensile state CANISO develops on the bedding plane.

5.1.3 External Benchmark

Validating the grid against a closed-form solution shows internal consistency, but it doesn't say whether the model behaves like other implementations of the same problem. There's a useful external check available here, because the synthetic case in Section 4.2: σ_{Hmax} = 30 MPa, σ_{hmin} = 20 MPa, pf = 11 MPa, pw = 12 MPa deliberately reuses the configuration Deangeli et al [6] and Liu et al [17] used for Tournemire shale, on the same code and the same style of radial grid. The rocks are different, but for the two elastic models the pore-pressure response depends on stiffness rather than strength, so the comparison still means something.

Table 5.3: Undrained pore pressure at the wall: present study (Songliao) against published Tournemire simulations [17], same far-field stresses, same pf and pw.

Model	**pf at Point A Songliao**	**pf at Point A Tournemire**	**pf at Point B, Songliao**	**pf at Point B, Tournemire**
ILE	5.94 MPa	7.0 MPa	16.16 MPa	14.0 MPa
TIE	8.57 MPa	7.5 MPa	12.53 MPa	13.5 MPa

Agreement is within 2.2 MPa on every entry. More telling than the absolute match, though, is that both studies show the same direction of change when elastic anisotropy is introduced: moving from ILE to TIE lowers the over-pressure at Point B and raises the under pressure at Point A in both cases, compressing the dipole. The elastic constants of the two shales aren't identical, so exact agreement was never expected, what this comparison establishes is that the undrained coupling implemented here behaves consistently with an independently built model of the same problem. From here on the grid is treated as validated, the dry protocol is used later, and every result in Sections 5.2 – 5.6 is undrained.

5.2 Elastic Anisotropy: the TIE Model

TIE keeps the matrix perfectly elastic and unable to fail, just like ILE, but swaps the two isotropic constants for the five in Table 4.4: E_1 = 10 GPa parallel to bedding, E_2 = 4.9 GPa perpendicular, a stiffness ratio of 2.04. Running it on the same validated grid and boundary conditions from Section 5.1 isolates the effect of elastic anisotropy on its own.

Table 5.4: TIE against the ILE baseline, undrained, at the borehole wall.

Quantity	**ILE (baseline)**	**TIE**	**Δ (TIE − ILE)**
σ_θ at Point A	18.40 MPa	20.49 MPa	+2.09 MPa
σ_θ at Point B	57.22 MPa	61.12 MPa	+3.90 MPa
pf at Point A	5.94 MPa	8.57 MPa	+2.63 MPa
pf at Point B	16.16 MPa	12.53 MPa	- 3.63 MPa
Skempton dipole Δpf	10.22 MPa	3.963 MPa	- 6.26 MPa
Effective σ_θ' at Point B	41.06 MPa	48.59 MPa	+7.53 MPa

Total hoop stress goes up at both azimuths, more so at Point B than at Point A, the mechanism here is standard: bedding is softer across its own plane than along it, so the rock deforms more easily normal to bedding, and to keep equilibrium around the opening the redistributed stress concentrates more where the softer direction is carrying the load. What's specific to this case is how big the effect is around 6% on a wall stress near 61 MPa, large enough to flip a failure prediction, since it pushes σ_θ' across the matrix strength threshold discussed next. The Skempton dipole tells a different story: its amplitude drops from 10.22 MPa to 3.96 MPa, because the stiffer bedding-parallel direction distributes volumetric strain more evenly around the wall and moderates the local pore pressure swing at each azimuth. Despite that, the effective hoop stress at Point B comes out higher than ILE, the total stress amplification outweighs the poro elastic relief.

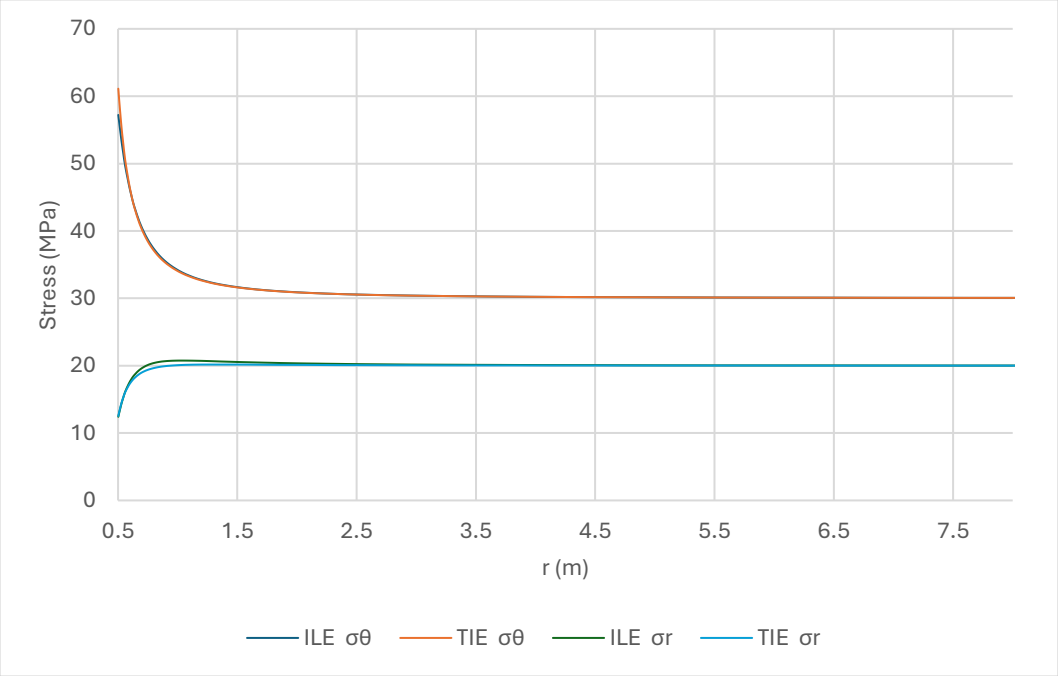


Figure 15: Radial profiles of σ_θ and σ_r from the wall to the far field at Point B, ILE against TIE, undrained.

Figure 15 shows something the wall-value table alone can't. The ILE and TIE hoop-stress curves stay close but are distinguishable at this scale, with TIE consistently above ILE, consistent with the ~6% difference between them, and both decay toward the far field as expected. The radial stress curves show a small overshoot: both models rise about 0.8 MPa above the far-field value of 20 MPa near r = 1 m before settling back down. This isn't a numerical artefact; it's a real feature of the underlying Kirsch solution, and the simulation reproduces it almost exactly.

Matching that detail is a stronger check than the two wall points in Table 5.1 alone: it confirms the model tracks the Kirsch solution across the whole radial profile, not just at the wall which matters, since every model later in this chapter is read the same way.

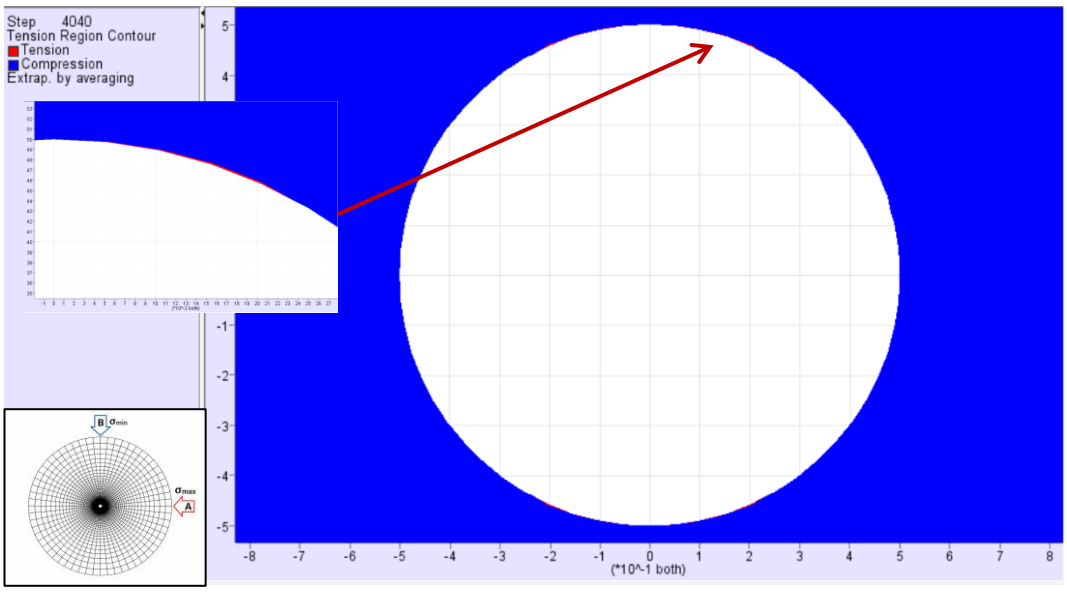


Figure 16: Tension/compression state of the wall, TIE undrained (red = tension, blue = compression).

Figure 16 turns the mechanism derived algebraically in Section 5.1.2 into something you can see. Small red caps sit at the wall at Point B and, symmetrically, at θ = 270°; everywhere else, including all of Point A, the rock is in compression. The location matters here: a contouring or mesh-grading artefact would have no reason to show up exactly at the azimuth where the undrained overpressure peaks and nowhere else, and it wouldn't stay confined to the first zone at the wall. What the figure shows here is the signature Eq. 2.7a predicts with the locally computed pore pressure, $\sigma_r{}'$ goes negative only where pf exceeds pw, and only there. With pf = 12.53 MPa against pw = 12 MPa, the overpressure is only 0.53 MPa, which is why the tension caps are so small and stay pinned to the wall. The algebra from Section 5.1.2 and this contour aren't fully independent checks, since both come from the same computed pore pressure field, but together they make the radial-tension mechanism a result of the study rather than something argued for on paper alone.

TIE doesn't have a failure criterion, so there's no zone-state map for this model, its role here is just to give a reference value. At Point B, the effective hoop stress comes out to $\sigma_\theta{}'$ = 48.59 MPa. This is the stress the wall would see if the rock were elastically anisotropic but still couldn't fail. This value is already higher than the matrix compressive strength C_0 = 44.2 MPa, and it's 7.53 MPa higher than what the isotropic model gave. So just by adding elastic anisotropy, without changing the

strength of the rock at all, the predicted stress goes from below the failure threshold to above it. This shows that elastic anisotropy on its own can matter for wellbore stability, even before any failure criterion is applied. It supports the point made earlier in the chapter that shale shouldn't be treated as elastically isotropic.

5.3 Matrix Plasticity: the ILE - MC Model

ILE-MC goes back to isotropic elasticity but adds the Mohr-Coulomb criterion from Section 2.6.3, using the parameters from Table 4.5 (c'= 13.8 MPa, ϕ'= 26°, T_0 = 4.4 MPa, ψ = 0°, giving C_0 = 44.2 MPa). It's the first model in the hierarchy that can produce irreversible deformation, and the first one that can be checked against an analytical failure bound instead of just an elastic reference.

The analytical bound Combining the Kirsch solution with the Mohr–Coulomb criterion gives the mud pressure at which the matrix first yields at a given azimuth. Taking σ_θ'as the major and σ_r' as the minor effective principal stress at the wall a reasonable approximation near Point B, where σ_θ' dominates and substituting Eqs. 2.7a and 2.7g into Eq. 2.9 gives the standard collapse-pressure expression, the same one Deangeli et al. [6] use for this configuration:

$$P_{w\,MC} = \left[S - C_0 + P_f\left(N_\phi - 1\right)\right] / \left(N_\phi + 1\right), \quad S = \sigma_{Hmax} + \sigma_{hmin} - 2(\sigma_{Hmax} - \sigma h_{min}) \cos 2\theta$$

At Point B (θ = 90°), S = 70 MPa. With N_ϕ = 2.56 from ϕ' = 26°, C_0 = 44.2 MPa, and pf = 11 MPa, this gives pw-MC = 12.08 MPa. The simulations ran at pw = 12 MPa, 0.08 MPa (about 0.7% below that). So, the matrix at Point B is predicted to be marginally past yield: not comfortably elastic, not deeply plastic, sitting almost exactly on the yield surface. That's a useful place to be, since it's where differences between constitutive models show up most clearly. It's also worth flagging that this estimate is optimistic, it uses the far-field pf = 11 MPa rather than the higher local value the undrained coupling produces near Point B (Table 5.5), so the real margin is smaller than 0.08 MPa and could already be negative.

Table 5.5: ILE-MC, undrained, at the borehole wall.

Quantity	**Value**
σ_θ at Point A	18.23 MPa
σ_θ at Point B (wall)	50.81 MPa *

Quantity	Value
σ_θ at Point B (arch peak)	53.62 MPa at r = 1.07 Rw
pf at Point A / Point B	5.93 / 14.59 MPa
pf peak at Point B	15.72 MPa at r = 1.07 Rw
Effective σ_θ' at Point B (wall)	36.22 MPa

** Post-plastic-correction value: the stress reported after FLAC2D has applied the Mohr - Coulomb return mapping, not the elastic trial stress.*

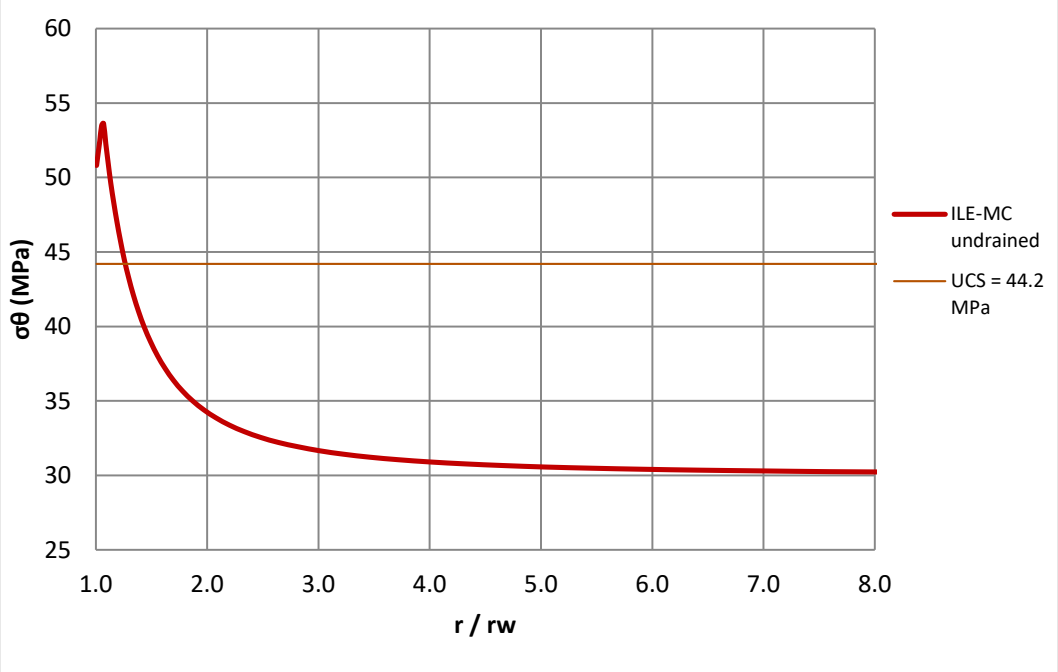


Figure 17: Radial profile of σ_θ at Point B for ILE-MC

The main thing to see in Figure 17 is the stress arch: the hoop stress no longer peaks right at the wall, as it does in every elastic model, but a short distance into the rock, at r = 1.07 Rw. This is the geometric fingerprint of matrix plasticity. Once the material yields it can't carry more load than its strength allows, so the excess gets shed outward until it reaches rock that's still elastic, and the peak moves into the formation.

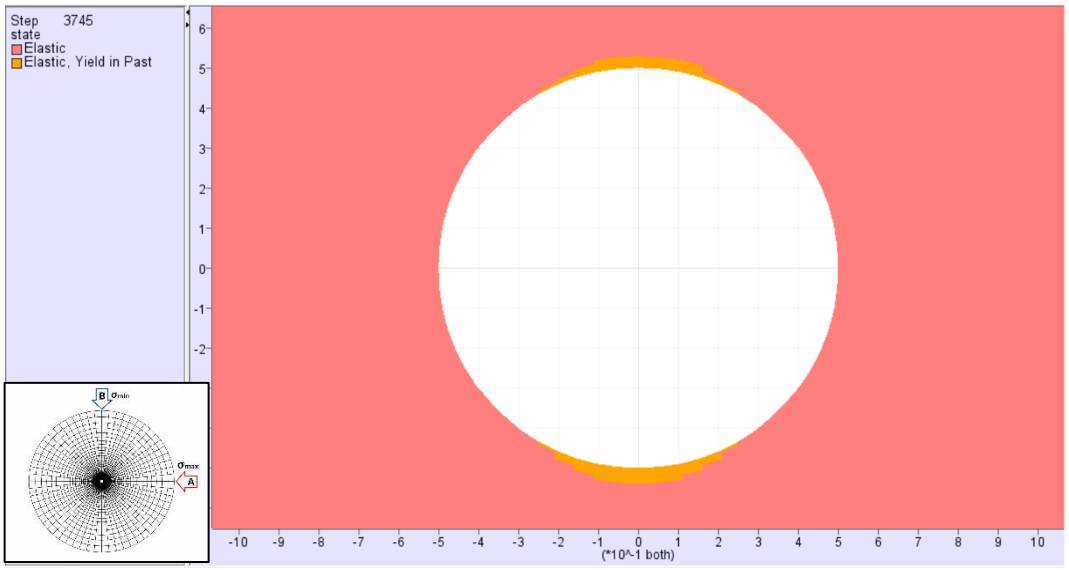


Figure 18: Zone state (plasticity) map, ILE-MC undrained.

Figure 18 confirms the analytical bound more clearly than the stress profile does. The state legend only has two entries: Elastic and Elastic, Yield in Past. No zone is still actively yielding once equilibrium is reached: every zone that crossed the yield surface during the iterative solve has since unloaded back into the elastic domain, leaving only a thin band of yield-in-past memory at the wall around Point B and, symmetrically, θ = 270°, spanning roughly ± 20°. Sector A, at σ_θ = 18.23 MPa against C_0 = 44.2 MPa, is elastic throughout with no yield markers at all.

Figure 18 also shows a specific pattern that tells us something useful. If the wall were well below its collapse pressure, there would be no yielding at all. If it were well above it, there would be a wide band of yielding all around it. What we see is neither of those extremes: a small amount of yielding right at the point of failure, which then settles down as the model reaches equilibrium. This matches the analytical prediction well: the closed-form solution gives a collapse pressure of pw-MC = 12.08 MPa, only 0.08 MPa above the applied 12 MPa. So, the numerical model, solved completely independently, lands on almost the same marginal result as the analytical formula predicts. This is the strongest agreement between the analytical work in Chapter 2 and the numerical results in Chapter 5, and it's why the analytical formulas are trusted later, in Section 5.7, to extrapolate beyond the pressures simulated.

It's also worth pointing out that the wall stress in this model, 36.22 MPa, is the lowest of all five models; even lower than the purely elastic case (41.06 MPa). This

is because matrix plasticity relieves stress at the wall. As the next sections show, every model added after this one brings some of that stress back.

5.4 Bedding Plane Slip: the UBI Model

UBI keeps the full ILE-MC matrix and adds a horizontal weak plane with its own weaker Coulomb strength parameters (Table 4.6:$c'_w = 3.7\text{MPa}, \phi'_w = 21°, T_0 = 3$ MPa) cohesion at about 27% of the matrix value, friction angle 5° lower. As described in Section 4.3.4, FLAC2D checks the matrix criterion first, applies any plastic correction, and only then tests the joint against the corrected stress, so matrix yielding can affect slip, but not the other way around within a single step. This is the first model where the two failure mechanisms from Section 2.6 can compete.

Table 5.6: UBI against ILE-MC, undrained, at the borehole wall.

Quantity	**ILE-MC**	**UBI**	**Δ**
σ_θ at Point A	18.23 MPa	16.66 MPa	- 1.57 MPa
σ_θ at Point B (wall)	50.81 MPa *	56.52 MPa	+5.71 MPa
σ_θ at Point B (peak)	53.62 @ 1.07 Rw	56.52 at the wall	arch removed
pf at Point B	14.59 MPa	11.54 MPa	- 3.05 MPa
Effective σ_θ' at Point B	36.22 MPa	44.98 MPa	+8.76 MPa

The important result of this section is right there in the third row of Table 5.6 and in figure 19, adding the weak plane removes the stress arch. UBI hoop stress peaks at the wall itself and decays outward monotonically, with no interior maximum. Physically, the joint acts as a second, weaker release mechanism working in a different direction Matrix plasticity relieves the wall by shedding load radially into the formation, which is what builds the arch in the first place; bedding-plane slip sheds load azimuthally, along the bedding, and does it efficiently enough that the radial mechanism never has to kick in. The rock reaches equilibrium without redistributing stress outward and so without relieving the wall.

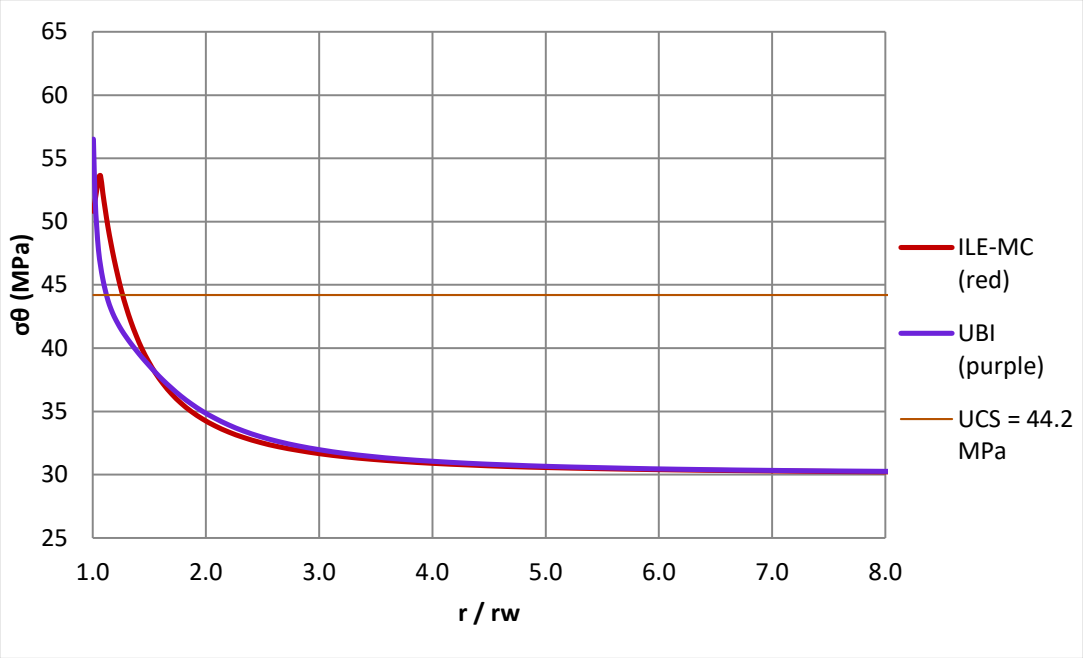
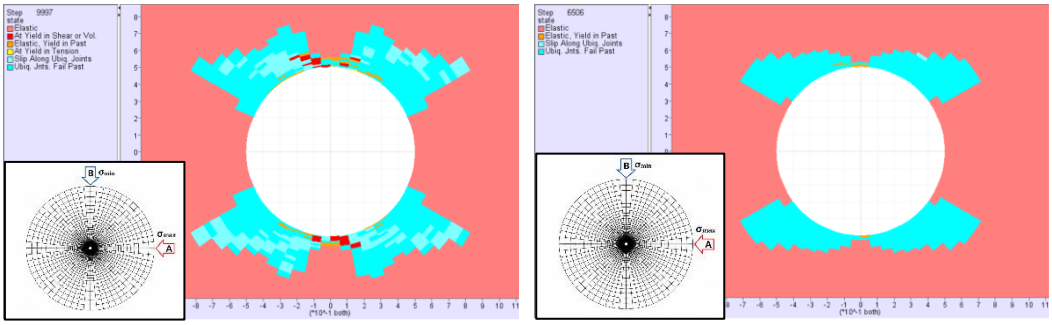


Figure 19: Radial profile of σ_θ at Point B, UBI (purple) against ILE-MC (red), with the UCS = 44.2 MPa reference line.

This point matters because it runs against the intuition that adding a failure mechanism should make a wellbore safer. UBI's effective hoop stress at Point B is 44.98 MPa against ILE - MC's 36.22 MPa, the model with two failure mechanisms predicts a wall stress 8.76 MPa higher than the model with one. Away from the wall the ranking flips: beyond about 1.5 Rw, both UBI curves in Figure 19 sit below both ILE - MC curves, converging near 31- 32 MPa against 35 - 40 MPa. So, the joint does lower the stress almost everywhere, just not at the one location that matters most.



(a) UBI, pw = 0 (dry) *(b) UBI, undrained, pw = 12 MPa*

Figure 20: Zone state map UBI: Panel (a) is the dry case pw = 0 panel (b) is the undrained case pw = 12 MPa.

Figure 20 (b) shows where the slip happens, and the geometry doesn't match a naive reading of "failure concentrates at Point B". Joint slip forms two lobes flanking each pole, separated by a narrow notch right at θ = 90° and 270° that's not occupied by any joint state but by the matrix legend: a thin sliver of Elastic, Yield in Past, the same marginal yield signature already seen in the ILE - MC map of figure 18, which makes sense since the two models share a matrix. Slip is least likely exactly where the hoop stress is highest.

The explanation is kinematic, and it reads straight off Eq. 2.10. At the wall the shear stress $\tau_{r\theta}$ is zero at every azimuth, so σ_r and σ_θ are the principal stresses themselves. With horizontal bedding, the angle βw between the bedding normal and the major principal stress equals the azimuth θ. At Point B, βw = 90°: the bedding normal lines up with a principal direction, the resolved shear on the plane is zero, and Eq. 2.10 goes singular: slip can't happen, exactly as Section 2.6.4 says for βw near 0° or 90°. Moving away from the pole, βw drifts from 90°, resolved shear grows from zero, and the hoop stress is still near its maximum. What the state map adds is that the notch at the pole doesn't stay intact, the matrix fails there instead, since UBI's matrix (unlike CANISO's) can fail, and it does so exactly where the joint can't. The two mechanisms cover different azimuths, and between them nothing in the loaded sector escapes undamaged.

Comparing the two panels of Figure 20 raises a question this study can't fully answer. The pw = 0 map shows a much more extensive slip pattern than the pw = 12 MPa map, reaching out to roughly 1.4 - 1.5 Rw where the undrained case stays confined to tight caps barely past the wall. Part of that is expected, mud pressure suppresses failure, and that reduction is the whole point of Section 5.7.2 but the undrained case also carries elevated pore pressure, which lowers the effective normal stress on the joint and, through the frictional term in Eq. 2.10, should promote slip rather than suppress it. The two effects pull against each other, and the mud pressure clearly wins out. The most plausible explanation is that slip extent depends on the driving shear stress integrated over an annulus rather than on conditions at the wall alone. In the dry run the hoop stress is higher across the whole near-wall annulus (Figure 19), so more zones reach the slip criterion of Eq. 2.10 even though the absence of pore pressure raises the effective normal stress that resists slip; the wider driving-stress field outweighs both the higher joint resistance and the pore-pressure term that would otherwise favour the undrained case. Figure 19 shows the undrained hoop-stress profile sitting below the pw = 0 profile almost everywhere outside the first zone. That's a hypothesis the data is consistent with, not something demonstrated here; separating the mud pressure effect from the pore pressure effect would need a run at pw = 12 MPa with the pore pressure held uniform, a single extra simulation listed among the open items in Section 5.10.

5.5 Anisotropic Elasticity with Weak-Plane Slip: the CANISO Model

CANISO combines the transversely isotropic elasticity from Section 5.2 with the same weak plane as UBI, but drops the matrix strength entirely, in Section 4.3.5, the matrix has no cohesion, friction angle, or tensile cutoff, and can't yield under any stress. All plasticity is joint slip, evaluated directly on the anisotropic stress state without a prior matrix correction, the opposite algorithmic order from UBI. So, the model answers a specific question: what does the weak plane do when it's the only thing that can fail?

Table 5.7: CANISO, undrained, at the borehole wall.

Quantity	**Value**
σ_θ at Point A	19.02 MPa
σ_θ at Point B	63.04 MPa (wall = peak)

Quantity	Value
pf at Point A / Point B	7.95 / 12.07 MPa
Effective σ_θ' at Point B	50.97 MPa

CANISO produces the most severe wall stress of any model in the hierarchy: σ_θ' = 50.97 MPa at Point B, higher even than TIE's purely elastic 48.59 MPa. Two effects stack up here. Anisotropic stiffness amplifies the elastic stress concentration, as already established in Section 5.2; and with no matrix plasticity, there's nothing to cap it, because the joint can only relieve stress where it's favourably oriented which, per Section 5.4, doesn't include the area right around Point B.

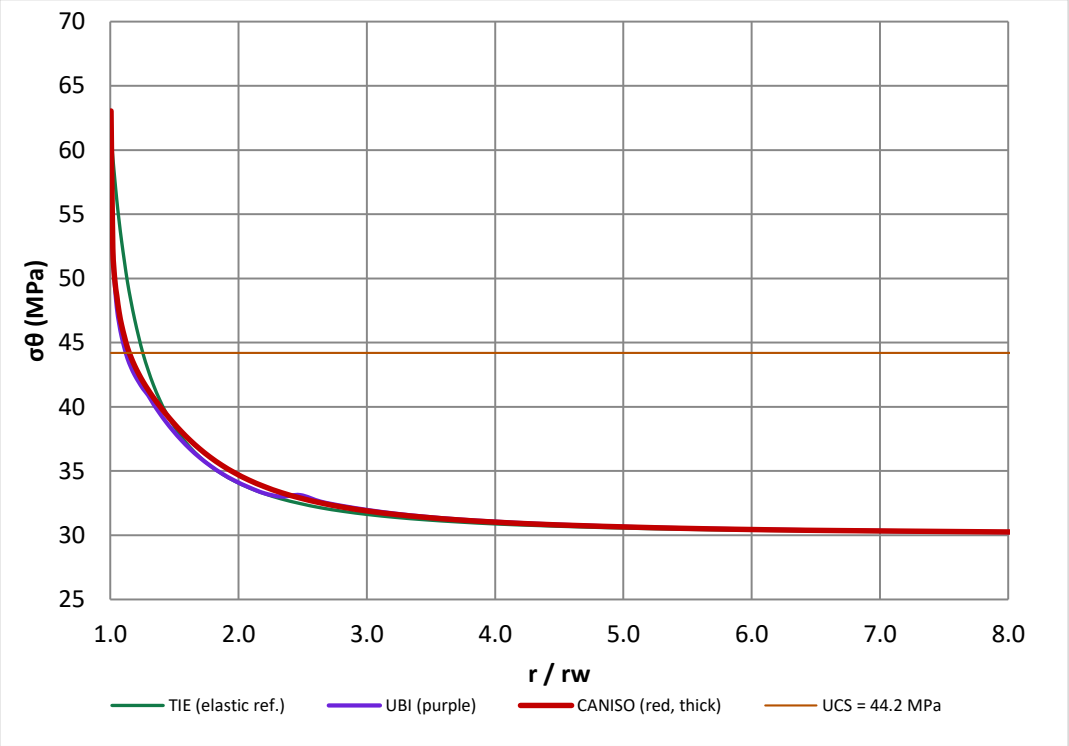
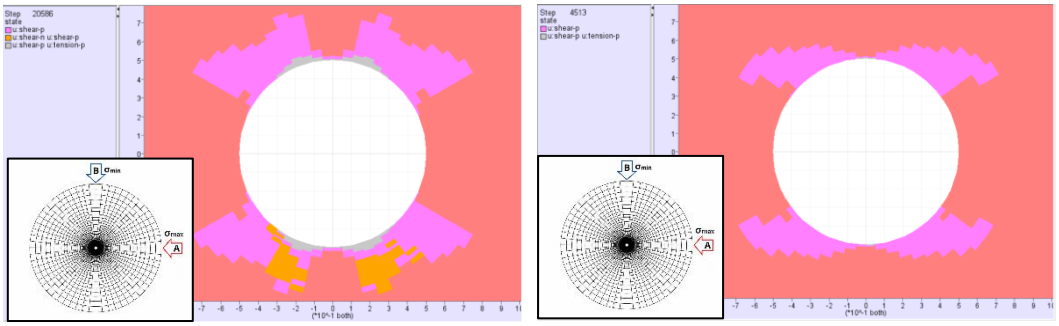


Figure 21: Radial profile of σ_θ at Point B: CANISO (red, thick) against TIE (green, elastic reference) and UBI (purple).

Figure 21 puts an important qualifier on that severity. The CANISO curves don't stay above TIE the way their wall values would suggest, they fall steeply within roughly the first half radius, cross below the TIE elastic reference around r = 1.3 - 1.5 Rw, and from there run almost on top of the UBI curves out to r = 8 Rw, with all four converging near 31 - 32 MPa. So CANISO's extreme wall stress is strictly

a near-wall effect. Once joint slip engages a short distance into the formation, it pulls the anisotropic stress state down onto essentially the same redistributed profile the isotropic matrix joint model produces, and the memory of the stiffness contrast disappears within one or two wellbore radii. Away from the wall, it's the joint not the elastic anisotropy that governs the redistribution.



(a) CANISO, pw = 0 (dry) *(b) CANISO, undrained, pw = 12 MPa*

Figure 22 : Zone state map, CANISO. Panel (a) dry (pw = 0), panel (b) undrained (pw = 12 MPa). Pink = joint shear slip (u:shear-p); grey = combined joint shear and tension (u:shear-p, u: tension-p) at the poles; orange (dry only) = mixed shear states. The matrix carries no failure state in either panel, confirming all plasticity is joint borne.

Figure 22 shows the same two-lobe pattern as Section 5.4, slip in symmetric lobes flanking each pole, but the notch between the lobes looks different here. In UBI, the matrix yielded at θ = 90°. In CANISO, the matrix can't yield at all, so what shows up there instead must be a joint state: a combination of shear and tension. In the state map this appears as the grey u: shear-p u:tension-p cells at each pole, distinct from the pink pure-slip lobes that flank them. This makes sense geometrically. With horizontal bedding, the plane normal at Point B points in the same direction as the radial stress, so the effective normal stress on the joint there is just σ_r'. That's the same quantity Section 5.1.2 showed goes into tension at this exact spot, once the undrained overpressure exceeds the mud pressure. The joint's tensile cutoff, T_{0w} = 3.0 MPa is well below the matrix value of 4.4 MPa, and Table 5.5 shows the near wall pore pressure reaching up to 15.72 MPa against an applied 12 MPa, easily enough to put σ_r' within reach of that lower cutoff. So, the tensile behaviour that came up earlier, in the validation section, as a small side detail of the elastic solution, turns out to control what happens at the most heavily loaded point on the wall.

This result also lines up closely with published work. Liu et al. [17] report tensile states in both their UBI and CANISO models of Tournemire shale, at orientations around θ = 90° ± 30°, locations they describe as "zones not prone to tension" under a simple isotropic reading. They conclude that this "underscores the need for careful estimation of weak plane tensile strength, a parameter often overlooked in practical applications due to a lack of suitable correlations with log data".

5.6 Comparison of the UBI and CANISO models

UBI and CANISO are the only two models here that carry the bedding plane, and they're built to be compared directly: they share the exact weak plane parameters from Table 4.6 and differ in only two respects: matrix elasticity (isotropic in UBI, transversely isotropic in CANISO) and matrix strength (Mohr - Coulomb in UBI, none in CANISO). So, any difference between them comes from those two changes, and pulling those contributions apart is the most useful thing this section can do.

Table 5.8: UBI against CANISO. Undrained values are the results of Sections 5.4 and 5.5; the pw = 0 row is included because it isolates the matrix-strength difference most sharply (Section 5.7.2).

Quantity	**UBI**	**CANISO**	**Δ (CANISO − UBI)**
σ_θ at Point A, undrained	16.66 MPa	19.02 MPa	+2.36 MPa
σ_θ at Point B, undrained	56.52 MPa	63.04 MPa	+6.52 MPa
Effective σ_θ' at Point B	44.98 MPa	50.97 MPa	+5.99 MPa (+13.3 %)
pf at Point A / Point B	5.51 / 11.54 MPa	7.95 / 12.07 MPa	dipole 6.03 → 4.12 MPa
σ_θ at Point B, pw = 0	43.47 MPa *	91.38 MPa	+47.91 MPa (× 2.10)
Failure mechanisms available	matrix + joint	joint only	/

* *Post-plastic-correction value.*

Under undrained conditions the two models differ by 13.3 % in effective hoop stress at Point B. That difference is smaller than the 18.3 % measured between ILE and

TIE in Section 5.2, which bounds the contribution elastic anisotropy can make. Most of the undrained gap between UBI and CANISO is therefore attributable to elastic anisotropy rather than to the difference in matrix strength. The pw = 0 row tells a different story: CANISO predicts 91.38 MPa against UBI's 43.47 MPa, a factor of 2.10, which elastic anisotropy alone cannot account for. The difference follows from the matrix criterion. UBI's matrix yields and caps the hoop stress at its uniaxial compressive strength: with $\sigma_3' = 0$ the Mohr-Coulomb criterion limits σ_1' to C_0 = 44.2 MPa, and the simulated value is 43.47 MPa. CANISO has no matrix criterion and carries no equivalent cap. The value it returns is more than twice C_0 and is therefore not a stress the rock could sustain; it is a property of a model without a matrix criterion rather than a prediction of wall stress.

This is a genuine limitation of CANISO as a stability tool. The model is internally consistent, it behaves exactly as Section 4.3.5 describes, but it is reliable only where the matrix remains close to elastic. At pw = 12 MPa that condition is nearly met, since Section 5.3 showed the matrix only marginally past yield, which is why the undrained gap remains modest. At pw = 0 the condition fails. CANISO is therefore useful only when the matrix is close to elastic, and that must be verified with a model that carries a matrix criterion: ILE-MC or UBI must be run alongside CANISO rather than in place of it.

The two models also differ in the failure mode they predict, which for wellbore stability matters more than the magnitude of the stress. UBI predicts a mixed mechanism: bedding slip over two broad lobes flanking each pole, with matrix breakout occupying the narrow notch at the pole where slip is kinematically excluded. CANISO predicts slip wherever the joint orientation allows it, together with a combined shear and tensile state in the notch, and no matrix failure anywhere. Breakout at the pole is a localised, self-limiting enlargement of the hole, managed by hole cleaning and mud weight; distributed slip along bedding produces the tabular cavings characteristic of laminated shale, which are associated with pack-off and stuck pipe rather than with simple hole enlargement [2]. UBI predicts both mechanisms and is therefore the more complete diagnostic; CANISO predicts the more severe near-wall stress and is best used as an upper bound. The recommendation carried into Section 5.7 is to use UBI as the working model and CANISO as a stress envelope.

One more contrast is worth flagging because it cuts against expectation. CANISO produces a smaller pore-pressure dipole than UBI (4.12 vs. 6.03 MPa) but a higher effective stress at Point B, the same pattern already seen between TIE and ILE in

Section 5.2, and for the same reason: anisotropic stiffness spreads volumetric strain more evenly around the wall, which moderates the pore-pressure swing, but at the same time amplifies the total stress by more than that poroelastic relief is worth. A smaller dipole isn't, by itself, a sign of a more stable wellbore. Any assessment that tracks excess pore pressure without also tracking the total stress it's modifying will get the ranking backwards.

5.7 Mud Weight Window and Drilling Implications

Sections 5.2 to 5.6 describe how the rock responds at one mud pressure. Section 2.7 defined the practical objective differently: the range of mud pressures within which the well can be drilled at all, and it identified two questions to answer how much pressure the matrix requires, and how that compares with the pressure the bedding planes require. The first has already been answered analytically in Section 5.3. The second is answered here from the simulations themselves.

The matrix bound was obtained in Section 5.3 by substituting the far-field stresses of Table 4.1 and the strength parameters of Table 4.5 into Eq. 2.9, giving pw-MC = 12.08 MPa at Point B. The simulations were run at pw = 12 MPa, 0.08 MPa below it, and Figure 18 confirmed the prediction: the matrix shows only transient, recovered yielding at the wall and no zone still at yield when the model reaches equilibrium. For the intact rock, in other words, the applied mud pressure is marginal but very nearly adequate a driller working from the Mohr - Coulomb criterion alone would raise the mud weight slightly and consider the problem solved.

The state maps of Sections 5.4 and 5.5 show that this would be a serious misreading, and they show it without any further calculation. At the same mud pressure of 12 MPa at which the matrix is only marginally past yield, joint slip in both UBI and CANISO extends over broad lobes covering a large part of the wall. The two mechanisms are being observed under identical conditions, so the comparison is direct: the mud pressure that leaves the matrix on the edge of yielding leaves the bedding planes far past it. The pressure required to suppress bedding slip is therefore substantially higher than the 12.08 MPa required to suppress matrix shear. This is the comparison Section 2.7 called for, and the answer for the Songliao shale is unambiguous the bedding planes, not the intact rock, set the collapse limit for this wellbore.

The magnitude of that gap is not quantified here. Establishing it would require evaluating Eq. 2.10 for the mud pressure at slip across the full range of azimuths

and bedding angles, which is a sensitivity analysis in its own right of the kind carried out by Deangeli et al [6], and it is identified in Section 5.10 as the natural continuation of this work. What the present results establish is the direction and the governing mechanism, which is what the choice of a mud weight depends on first.

5.7.1 Sensitivity to Mud Pressure

The simulations provide a second point on the pressure axis. The pw = 0 runs, introduced in Section 5.1 as the dry validation protocol and set aside there, are mechanically also the zero mud pressure end member of the same problem, and reading them that way turns a validation artefact into the sensitivity analysis promised in Section 4.4. The comparison is not clean the pw = 0 runs also have pf = 0, so mud pressure and pore pressure change together but the direction of the effect is unambiguous and consistent across all five models.

Table 5.9: Hoop stress at Point B at the two simulated mud pressures. The pw = 0 column also has pf = 0.

Model	**σ_θ at B, pw = 0**	**σ_θ at B, pw = 12 MPa**	**Peak location, pw = 0 → 12 MPa**
ILE	69.01 MPa	57.22 MPa	wall → wall
TIE	72.90 MPa	61.12 MPa	wall → wall
ILE-MC	44.58 MPa *	50.81 MPa *	1.16 Rw → 1.07 Rw
UBI	43.47 MPa *	56.52 MPa	1.09 Rw → wall
CANISO	91.38 MPa	63.04 MPa	wall → wall

** Post-plastic-correction value.*

For the three models without matrix plasticity the effect is straightforward: raising the mud pressure to 12 MPa lowers the Point B hoop stress by 12 - 28 MPa, and the reduction is largest for CANISO, which had the most stress to shed. The two models with a matrix criterion behave in the opposite direction at the wall, because their pw = 0 wall values are not elastic stresses at all but post-yield capped values the matrix had already failed and could carry no more. Reading Table 5.9 without that

distinction would suggest that mud pressure increases the load on the wall in ILE-MC and UBI, but the correct comparison for those two models is the extension of the damaged zone: the ILE-MC arch peak migrates inward from 1.16 Rw to 1.07 Rw, and the UBI slip lobes in Figure 20 contract from roughly 1.4 - 1.5 Rw to tight caps barely past the wall. Mud pressure shrinks the failed zone in the same way the state maps of Liu et al. [17] show for Tournemire shale.

5.7.2 Practical Implications

Three observations follow for the drilling of a well of this kind, and they are worth separating because they point in different directions:

- Increasing the mud weight does improve stability, but the criterion used to calculate it must be chosen properly. Table 5.9 shows that going from 0 to 12 MPa lowers the hoop stress at Point B in all five models, and Figure 20 shows the slipped zone shrinking from about 1.4 - 1.5 Rw to a thin cap at the wall, so mud weight clearly works. The difficulty is the value chosen. The Mohr-Coulomb criterion applied to the intact rock is 12.07 MPa (Section 5.3), and at that pressure the matrix is indeed only just at yield. The same pressure, however, leaves the bedding planes slipping over wide sectors of the wall in both UBI and CANISO. The mud pressure that is enough for the matrix is not enough for the bedding. For this formation, with horizontal bedding, it is safer to set the lower limit of the mud weight window based on the weak planes.

- The models also predict different types of failure, which is very important for wellbore stability studies. ILE-MC gives breakout in the rock matrix, in a narrow band at Point B and at $\theta = 270°$. UBI and CANISO give slip along the bedding over much wider parts of the wall. The two cause different problems during drilling. A breakout widens the hole in one direction and then stops, and it is usually handled by cleaning the hole and raising the mud weight. Slip along the bedding loosens fragments from the wall, which can fall into the hole, block it, and trap the drill string.

- These results describe the first hours after drilling. All the runs are undrained, so the pore pressure field in Table 5.2 is the one present immediately after the bit passes, before the fluid has had time to move. Section 5.1.2 showed that this is the worst moment at Point B: the pore pressure there rises above its initial value, which lowers the effective stress holding the rock against shear failure. Once the excess pressure drains away

the effective hoop stress recovers, so the hole is most exposed in the early hours and limiting the open hole time is an important parameter to take into consideration.

5.8 Cross Model Synthesis

Table 5.10: All five constitutive models, undrained protocol, at the borehole wall.

Quantity	ILE	TIE	ILE-MC	UBI	CANISO
σ_θ at Point A	18.40	20.49	18.23	16.66	19.02
σ_θ at Point B	57.22	61.12	50.81 *	56.52	63.04
Peak location	wall	wall	1.07 Rw	wall	wall
pf at Point A	5.94	8.567	5.93	5.51	7.95
pf at Point B	16.16	12.53	14.59	11.54	12.07
Effective $\sigma_\theta{}'$ at B	41.06	48.59	36.22	44.98	50.97

All stresses in MPa. * Post-plastic-correction value.

Read across the last row of Table 5.10 shows the quantity that governs shear failure the five models rank: ILE-MC (36.22) < ILE (41.06) < UBI (44.98) < TIE (48.59) < CANISO (50.97). That is not the order of their constitutive complexity, and the departure is systematic rather than accidental. The two isotropic models sit at the bottom: the matrix either caps the wall stress or never inflates it in the first place. The two anisotropic models sit at the top, because elastic anisotropy amplifies total stress before any failure mechanism has the chance to relieve it. UBI sits between them, above the isotropic plastic model despite sharing its matrix, because the joint removes the arch that was providing the relief. The generalisation the table supports is that adding a failure mechanism does not make the wall safer it changes where and how the rock redistributes stress, and depending on the mechanism the wall can end up better off (ILE - MC), worse off (UBI), or governed by something else entirely (CANISO).

Two qualifications limit how far that ranking should be carried. The first is spatial: it is a wall value ranking, and Figure 21 showed CANISO and UBI becoming indistinguishable a few radii out. A comparison of constitutive models for wellbore stability must specify where it is being made, because the ordering is not stable with distance from the wall. The second is that the ranking is by stress, not by hazard. CANISO reports the highest stress but the least complete failure inventory; ILE-

MC reports the lowest stress. The model that predicts the most benign stresses is not the model that predicts the most benign well.

The pore pressure response, by contrast, is qualitatively identical across all five models: under-pressure at Point A, over-pressure at Point B, in every case. This is expected given that the dilation angle is zero for every matrix and every joint in this thesis ($\psi = 0$ throughout Tables 4.5 and 4.6). With no plastic volumetric strain to speak of, the poro elastic response is driven by the elastic mean stress redistribution described in Section 5.1.2, and the models differ in how tightly the dipole is focused rather than in the mechanism producing it. With the dipole magnitude ranges from 3.96 MPa (TIE) to 10.22 MPa (ILE) while the effective-stress ranking runs in the opposite direction, this confirms once more: the pore-pressure response cannot be read as a stability indicator on its own.

5.9 Comparison with Other Shales

The synthetic case of Section 4.2 was chosen to match the configuration used for Tournemire shale by Deangeli et al. [6] and Liu et al. [17], so that differences between the two studies are attributable to the rock rather than to the loading. The Tournemire strength parameters are taken from the WPM regression of the laboratory data of Abdi et al. [1]; the bounds below are computed here with the same expressions used in Section 5.3, so the comparison is like for like.

Table 5.11: Songliao shale (this study) against Tournemire shale [1,6,17], same far-field stresses and pore pressure. The Tournemire matrix bound is computed here from the published parameters using Eq. 2.9, for comparison on the same basis.

Quantity	Songliao	Tournemire [1,6,17]
Matrix cohesion c' / friction ϕ'	13.8 MPa / 26°	8.37 MPa / 33°
Matrix UCS, C_0	44.2 MPa	30.8 MPa
Joint cohesion c'_w / friction ϕ'_w	3.7 MPa / 21°	4.26 MPa / 32°
Strength contrast c'_w / c'	0.27	0.51
Joint tensile cutoff T_{0w}	3.0 MPa	3.0 MPa
Matrix collapse bound (Eq. 2.9)	12.08 MPa	14.91 MPa

The comparison produces a result that is not obvious from the strength data alone. The Songliao matrix is substantially stronger than the Tournemire matrix: a uniaxial compressive strength of 44.2 MPa against 30.8 MPa (43 % higher) and its matrix collapse bound is correspondingly lower, 12.08 against 14.91 MPa. Judged on intact-rock strength alone, Songliao would be the easier well. The bedding tells the opposite story. The Songliao weak planes carry only 27 % of the matrix cohesion where the Tournemire planes carry 51 %, and their friction angle is 5° below the matrix where Tournemire's is barely 1° below. Relative to its own matrix, in other words, the Songliao fabric is by some margin the weaker of the two.

That contrast is consistent with what the simulations show. Section 5.7 established that at pw = 12 MPa the Songliao matrix is only marginally past yield while the bedding planes slip over a wide sector of the wall, so the fabric governs by a clear margin. The strength ratios in Table 5.11 suggest that the same calculation carried out for Tournemire would show the two mechanisms much closer together. The practical reading is that the penalty for ignoring bedding is formation-specific and cannot be carried from one shale to another on the basis of intact-strength similarity: it depends on the ratio between fabric and matrix strength, which is measured by a different test than the one that gives UCS. One caveat applies to the Tournemire column throughout. Deangeli et al. [6] show that the WPM regression used to obtain those weak-plane parameters fits the laboratory data poorly and overestimates the compressive strength at every bedding angle, so the Tournemire values are themselves uncertain and the contrast drawn here should be read as indicative rather than exact.

Beyond the direct benchmark, the qualitative behaviour reported here is consistent with the broader anisotropic wellbore literature reviewed in Chapter 1. The finding that a wellbore stability analysis treating shale as isotropic in either direction depending on azimuth or bedding orientation [3,19] is reproduced concretely in Table 5.10, where the isotropic models are the most optimistic of the five at Point B. The observation that tensile states develop along weak planes at azimuths not prone to tension on an isotropic reading [17] is reproduced in Figures 16 and 22. And the conclusion that neglecting undrained excess pore pressure leads to an underestimate of the required mud pressure [17] follows here directly from the asymmetry quantified in Section 5.1.2. Where the present study adds rather than confirms is in the magnitude: for this formation, the effects are large enough to change the answer, not merely to refine it.

5.10 Contribution and Limitations

The methodology applied in this thesis; a hierarchy of five FLAC2D constitutive models run on a common grid under a shared synthetic loading case, compared against the Kirsch solution and against the analytical criteria of the Weakness Plane Model, follows the approach developed for Tournemire shale by Deangeli et al. [6] and Liu et al. [17]. The contribution of the present work is not the framework, but what is done with it, and four results are specific to this study.

First, the framework is applied to the Qingshankou Formation of the Songliao Basin, a continental lacustrine shale whose mechanical parameters (Tables 4.3 – 4.6) differ materially from the marine argillite on which the method was developed. The comparison of Section 5.9 shows that this is not a routine substitution of inputs: the Songliao shale has the stronger matrix of the two but by some margin the weaker fabric relative to it, and it is the fabric that governs.

Second, the comparison promised in Section 2.7 is delivered for this formation: the mud pressure that leaves the matrix marginally past yield, 12.08 MPa from Eq. 2.9, leaves the bedding planes slipping over a wide sector of the wall. Collapse in the Songliao shale is therefore governed by the fabric and not by the intact rock, and a mud weight sized from the Mohr - Coulomb criterion alone would be materially unsafe. Quantifying the size of that gap is the natural continuation of the work and is identified as such among the limitations below.

Third, the location of bedding slip around the wall is explained rather than merely observed. Eq. 2.10 becomes singular where the bedding normal aligns with a principal stress direction, which at horizontal bedding occurs exactly at Point B; slip is therefore kinematically excluded at the most heavily loaded azimuth on the wall and must appear as lobes flanking it. Figures 20 and 22 show precisely that geometry, including the narrow unfailed notch at the pole. The agreement between a criterion from Chapter 2 and a finite-difference solution on a counter intuitive pattern is a stronger check on the weak-plane implementation than agreement on an expected one would have been.

Fourth, the mechanism behind the tensile state observed on the bedding plane at Point B is identified. Section 5.1.2 derives the effective radial tension from the undrained over-pressure exceeding the mud pressure; Figure 16 shows it in the continuum; Section 5.5 connects it to the joint, whose normal stress at that azimuth is σ_r', and whose lower tensile cutoff it reaches first. Liu et al. [17] report the phenomenon and note that it is not predicted by all elasto-plastic models; the present

work traces the chain from poroelastic coupling to weak plane tensile failure within a single formation and identifies the conditions under which it becomes active.

Against these, the limitations of the study should be stated precisely, since several of them bound how far the conclusions travel.

The numerical work is two-dimensional, plane-strain, and confined to a vertical well through horizontal bedding at $\delta = 0°$. Because the angle between the bedding normal and the principal stresses controls the slip criterion of Eq. 2.10, the results cannot be extrapolated to inclined bedding or to a deviated well without further analysis, and the conclusion that the fabric governs collapse is established for this geometry only. All results are undrained and short term; no drained companion analysis was run, so the long-term evolution of the pore-pressure field and its effect on stability is outside the scope of the conclusions. The dilation angle is zero for every material, which suppresses the plastic volumetric contribution to the pore pressure response and means the dipole reported here is the purely poro elastic one. One specific observation remains unresolved and is flagged rather than explained: the reduction of slip extent between the pw = 0 and pw = 12 MPa runs despite the higher pore pressure in the latter (Section 5.4). It is addressable with a single controlled run rather than with new physics. The most useful single extension, however, is to evaluate Eq. 2.10 for the mud pressure at slip across azimuth and bedding angle, in the manner of the sensitivity analyses of Deangeli et al. [6]: that would convert the qualitative finding of Section 5.7 into the numerical mud weight window that Section 2.7 sets as the ultimate objective. Finally, the strength parameters carry the uncertainty inherent in laboratory characterisation of shale discussed in Section 3.2; since the weak-plane parameters govern the collapse mechanism identified here, a formal sensitivity analysis on c'_w and ϕ'_w in the manner of [6] would be a prerequisite to using these numbers for any real well.

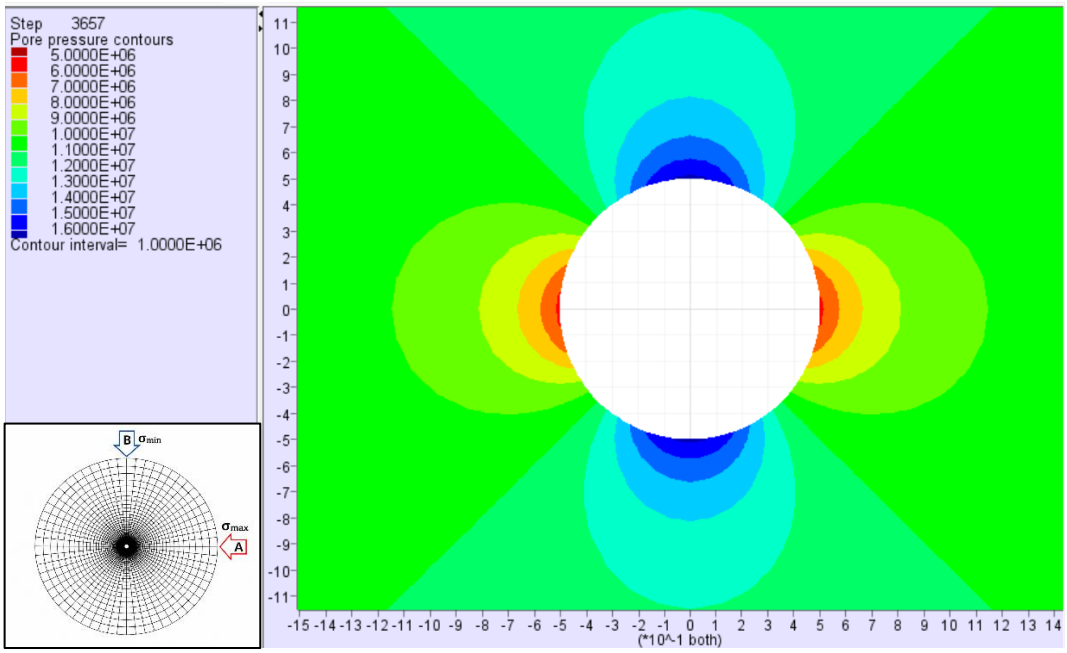


Figure 23: Pore fluid pressure contour map around the wellbore, undrained protocol.

Figure 23 confirms the Skempton dipole directly: pore pressure drops below the far-field 11 MPa along the σ_{Hmax} axis at Point A and rises above it along the σ_{hmin} axis at Point B, consistent with the values sampled at the two azimuths in Table 5.2. The perturbation stays confined to within a few wellbore radii of the wall, decaying back to the far-field value further out.

6. Conclusions

In this work, numerical models were carried out to study the stability of a wellbore drilled through the Qingshankou shale of the Songliao Basin. The analysis was carried out with FLAC2D on a single radial grid, keeping the far-field stresses, the pore pressure and the mud pressure of fixed and changing only the constitutive model, in five steps: ILE, TIE, ILE-MC, UBI and CANISO.

The first result is the validation of the model. The ILE model under the dry protocol gives 30.26 MPa at Point A and 69.01 MPa at Point B, against 30 and 70 MPa from the Kirsch solution. The error stays below 1.5% and comes from the fact that FLAC2D reports the stress at the centre of the zone and not exactly at the wall. Under the undrained protocol the pore pressures at the wall are within 2.2 MPa of the Tournemire results [17], obtained with the same stresses. The grid and the boundary conditions were therefore considered correct before comparing the models.

The second result is what each model adds. TIE now uses five elastic constants, with the rock twice as stiff along the bedding as across it (E_1 = 10 GPa, E_2 = 4.9 GPa). The strength is not modified, but the effective hoop stress at Point B rises from 41.06 to 48.59 MPa, that is 7.53 MPa or 18% more. The matrix strength is C_0 = 44.2 MPa, so the isotropic model puts the wall below the strength, and the anisotropic one puts it above. ILE-MC adds the Mohr-Coulomb criterion. Eq. 2.9 gives a collapse pressure of 12.08 MPa, very close to the 12 MPa applied, and the simulation agrees: only a thin band of about ±20° around Point B has yielded, and the stress peak moves into the rock at r = 1.07 Rw. The wall stress falls to 36.22 MPa, the lowest of the five models. UBI and CANISO give a different picture. At the same mud pressure, the bedding planes slip over two wide lobes on each side of Point B. They do not slip at Point B itself, because there the bedding is perpendicular to the maximum stress and the shear stress acting on the plane is zero. The weak plane is much weaker than the matrix, with a cohesion of 3.7 MPa, 27% of the matrix value, and a friction angle 5° lower. The bedding therefore slips while the matrix is only at the edge of yielding. The effective hoop stress at Point B ranks as ILE-MC (36.22) < ILE (41.06) < UBI (44.98) < TIE (48.59) < CANISO (50.97) MPa, which is not the order of complexity of the models. Matrix plasticity relieves the wall because it forms an arch, and bedding slip removes that arch. CANISO gives the highest value, but its matrix has no strength: at pw = 0 it gives 91.38 MPa, more than twice C_0. For this reason, CANISO can be used as an upper bound, together with UBI.

The third result is the comparison with the Tournemire shale [1,6,17], loaded in the same way. The Songliao matrix is stronger, with C_0 = 44.2 MPa against 30.8 MPa, and a lower matrix collapse bound 12.08 against 14.91 MPa. Looking only at the intact rock, Songliao would be the easier well. But its bedding planes carry only 27% of the matrix cohesion, while the Tournemire planes carry 51%. What matters therefore is the ratio between the weak plane and the matrix, and this ratio must be measured for each formation.

In conclusion, for the case studied here the mud pressure that keeps the matrix at the limit of yielding is not sufficient to prevent slip along the bedding, so the mud weight cannot be chosen only from the Mohr-Coulomb criterion. The pressure needed to stop the bedding slip was not calculated in this work. Evaluating Eq. 2.10 for all azimuths and bedding angles would provide it and would give the mud weight window defined as the objective in Section 2.7.

References

[1] Abdi, H., Labrie, D., Nguyen, T., Barnichon, J., Su, G., Evgin, E., Simon, R., & Fall, M. (2015). Laboratory investigation on the mechanical behaviour of Tournemire argillite. Canadian Geotechnical Journal, 52, 268-282. https://doi.org/10.1139/cgj-2013-0122

[2] Allawi, R. H., & Al-Jawad, M. S. (2021). Wellbore instability management using geomechanical modeling and wellbore stability analysis for Zubair shale formation in Southern Iraq. Journal of Petroleum Exploration and Production Technology, 11, 4047-4062. https://doi.org/10.1007/s13202-021-01279-y

[3] Cao, W., Liu, W., Liu, H., & Lin, H. (2022). Effect of formation strength anisotropy on wellbore shear failure in bedding shale. Journal of Petroleum Science and Engineering, 208, 109183. https://doi.org/10.1016/j.petrol.2021.109183

[4] Cao, Y., Yan, Q., Zhang, S., & Cai, F. (2024). Experimental research on anisotropy characteristics of shale under triaxial incremental cyclic loading and unloading. Applied Sciences, 14(6), 2602. https://doi.org/10.3390/app14062602

[5] Colak, K., & Unlu, T. (2004). Effect of transverse anisotropy on the Hoek-Brown strength parameter 'mi' for intact rocks. International Journal of Rock Mechanics and Mining Sciences, 41(6), 1045-1052. https://doi.org/10.1016/j.ijrmms.2004.04.004

[6] Deangeli, C., Liu, W., & Yang, K. (2024). Sensitivity analysis of wellbore mud pressure towards anisotropic shale properties, pore fluid pressure and far field stresses. Applied Sciences, 14(1), 148. https://doi.org/10.3390/app14010148

[7] Detournay, E., & Cheng, A. H.-D. (1993). Fundamentals of poroelasticity. In C. Fairhurst (Ed.), Comprehensive Rock Engineering: Principles, Practice and Projects (Vol. 2, Analysis and Design Methods, pp. 113-171). Pergamon Press.

[8] Dong, Q., Kang, J., Sun, J., Li, J., & Zhang, Z. (2024). Experimental study on anisotropic mechanical characteristics of shale under triaxial loading. Applied Sciences, 14(9), 3849. https://doi.org/10.3390/app14093849

[9] Gao, X., Wang, M., Shi, X., Dai, P., & Zhang, M. (2024). Wellbore stability research based on transversely isotropic strength criteria in shale formation. Soils and Foundations, 64(6), 101541. https://doi.org/10.1016/j.sandf.2024.101541

[10] He, W., Zhu, R., Cui, B., Zhang, S., Meng, Q., Bai, B., Feng, Z., Lei, Z., Wu, S., He, K., Liu, H., & Sun, L. (2023). The geoscience frontier of Gulong shale oil: Revealing the role of continental shale from oil generation to production. Engineering, 28, 79-92. https://doi.org/10.1016/j.eng.2022.08.018

[11] Hoek, E., & Brown, E. T. (1980). Empirical strength criterion for rock masses. Journal of the Geotechnical Engineering Division, 106(9), 1013-1035.

[12] Hu, F., Meng, Q., & Liu, Z. (2021). Mineralogy and element geochemistry of oil shales in the Lower Cretaceous Qingshankou Formation of the southern Songliao Basin, Northeast China: Implications of provenance, tectonic setting, and paleoenvironment. ACS Earth and Space Chemistry, 5(2), 365-380. https://doi.org/10.1021/acsearthspacechem.0c00336

[13] International Energy Agency. (2024). World Energy Outlook 2024. IEA, Paris. https://www.iea.org/reports/world-energy-outlook-2024. Licence: CC BY 4.0.

[14] Jaeger, J. C. (1960). Shear failure of anisotropic rocks. Geological Magazine, 97(1), 65-72. https://doi.org/10.1017/S0016756800061100

[15] Kirsch, G. (1898). Die Theorie der Elastizitat und die Bedurfnisse der Festigkeitslehre. Zeitschrift des Vereines Deutscher Ingenieure, 42, 797-807.

[16] Lame, G. (1852). Lecons sur la theorie mathematique de l'elasticite des corps solides. Bachelier.

[17] Liu, W., Deangeli, C., & Martinelli, D. (2024). Comparison of mud pressures predicted with different constitutive models in anisotropic shale rocks (Paper No. SPE-220041-MS). Society of Petroleum Engineers, SPE Europe Energy Conference and Exhibition, Turin, Italy. https://doi.org/10.2118/220041-MS

[18] Liu, X. J., Zeng, W., Liang, L. X., & Lei, M. (2016). Wellbore stability analysis for horizontal wells in shale formations. Journal of Natural Gas Science and Engineering, 31, 1-8. https://doi.org/10.1016/j.jngse.2016.02.061

[19] Ma, T., Liu, K., Qiu, Y., Liu, J., Martyushev, D. A., & Ranjith, P. G. (2025). Quantitative risk assessment of wellbore collapse of inclined wells in formations with anisotropic rock strengths. Rock Mechanics and Rock Engineering, 58, 1795-1818. https://doi.org/10.1007/s00603-024-04206-9

[20] Mahetaji, M., & Brahma, J. (2024). Prediction of minimum mud weight for prevention of breakout using new 3D failure criterion to maintain wellbore stability. Rock Mechanics and Rock Engineering, 57, 2231-2252. https://doi.org/10.1007/s00603-023-03679-4

[21] Mandal, P. P., Sarout, J., & Rezaee, R. (2022). Triaxial deformation of the Goldwyer gas shale at in situ stress conditions - Part I: Anisotropy of elastic and mechanical properties. Rock Mechanics and Rock Engineering, 55, 6121-6149. https://doi.org/10.1007/s00603-022-02936-2

[22] Terzaghi, K. (1936). The shearing resistance of saturated soils and the angle between the planes of shear. In Proceedings of the 1st International Conference on Soil Mechanics and Foundation Engineering (Vol. 1, pp. 54-56). Harvard University Press.

[23] U.S. Energy Information Administration. (2024, October 24).

[24] U.S. Energy Information Administration. (2026, May 11). The United States set record energy production in 2025, again. Today in Energy. https://www.eia.gov/todayinenergy/detail.php?id=67684

[25] Wu, W., Chan, C.-M., Su, X., Gu, Y., Liu, M., & Shao, W. (2025). Research on acoustic emission characteristics and mechanical properties of shale under uniaxial and conventional triaxial compression. Scientific Reports, 15, 12722. https://doi.org/10.1038/s41598-025-91189-4

[26] Yang, S.-Q., Yin, P.-F., Li, B., & Yang, D.-S. (2020). Behavior of transversely isotropic shale observed in triaxial tests and Brazilian disc tests. International Journal of Rock Mechanics and Mining Sciences, 133, 104435. https://doi.org/10.1016/j.ijrmms.2020.104435

[27] Sajjad Jalili, Kaveh Ahangari. Effects of different stress regimes on hydraulic fracture geometry: a particle flow code approach. Springer International Publishing AG 2017

[28] Seyed Pouyan Tahvildari, Soroush Shojaei & Mohsen Masihi. A physics-informed hybrid ML framework for pore pressure and fracture gradient prediction in carbonate reservoirs. Scientific Reports | (2026) https://doi.org/10.1038/s41598-026-41773-z

[29] Chiara Deangeli, Daniele Martinelli, DIATI Politecnico di Torino, Liu Wenjie, Department of Mining Engineering, Anhui University of Science and Technology. Failure pattern prediction in drilling anisotropic shales using analytical and numerical modelling.

[30] U.S. Energy Information Administration. (2011). Shale gas provides largest share of U.S.natural gas production (Today in Energy)

[31] Fjaer, E., Holt, R. M., Horsrud, P., Raaen, A. M., & Risnes, R. (2008). Petroleum related rock mechanics (2nd ed.). Elsevier. ISBN 978-0-444-50260-5.

[32] Li, S., Liang, K., Wang, C., Jiao, Y., Liu, H., & Wang, C. Study on the mechanism of anisotropic wellbore instability in continental shale in Songliao Basin. Journal of Petroleum Exploration and Production Technology, 12(9), 2551-2563, (2022).

[33] Li, S., Liang, K., Wang, C., Wang, Y., Jiao, Y., Zhu, X., & Wang, C. Study of wellbore instability and collapse mechanism for a layered continental shale oil horizontal well. Energies, 15(13), 4538, (2022).